ARTICLE

Check for updates

Magnonic superradiant phase transition

Motoaki Bamba [1,2,3 ✉], Xinwei Li[4], Nicolas Marquez Peraca[5] & Junichiro Kono [4,5,6]

In the superradiant phase transition (SRPT), coherent light and matter fields are expected to appear spontaneously in a coupled light–matter system in thermal equilibrium. However, such an equilibrium SRPT is forbidden in the case of charge-based light–matter coupling, known as no-go theorems. Here, we show that the low-temperature phase transition of $ErFeO_3$ at a critical temperature of approximately 4 K is an equilibrium SRPT achieved through coupling between Fe^{3+} magnons and Er^{3+} spins. By verifying the efficacy of our spin model using realistic parameters evaluated via terahertz magnetospectroscopy and magnetization experiments, we demonstrate that the cooperative, ultrastrong magnon–spin coupling causes the phase transition. In contrast to prior studies on laser-driven non-equilibrium SRPTs in atomic systems, the magnonic SRPT in $ErFeO_3$ occurs in thermal equilibrium in accordance with the originally envisioned SRPT, thereby yielding a unique ground state of a hybrid system in the ultrastrong coupling regime.

[1] The Hakubi Center for Advanced Research, Kyoto University, Kyoto 606-8501, Japan. [2] Department of Physics I, Kyoto University, Kyoto 606-8502, Japan. [3] PRESTO, Japan Science and Technology Agency, Kawaguchi 332-0012, Japan. [4] Department of Electrical and Computer Engineering, Rice University, Houston 77005, USA. [5] Department of Physics and Astronomy, Rice University, Houston 77005, USA. [6] Department of Material Science and NanoEngineering, Rice University, Houston 77005, USA. ✉email: bamba.motoaki.y13@kyoto-u.jp

In 1973, it was proposed[1,2] that *photon* and *matter* fields spontaneously appear in thermal equilibrium as a static transverse electromagnetic field and a static polarization, respectively, when the photon–matter coupling strength exceeds a certain threshold, entering the so-called ultrastrong coupling regime[3–5]. This phenomenon is known as the superradiant phase transition (SRPT) or Dicke phase transition, as the Dicke model was used in the theoretical calculations[1,2], having been originally developed to describe the superradiance phenomena[6].

The realization of the SRPT in thermal equilibrium may be expected to provide a new avenue for decoherence-robust quantum technology because the ground state of the Dicke model provides a quantum-squeezed vacuum on a photon–atom two-mode basis[7–11], and perfect ideal squeezing is obtained at the SRPT critical point, as recently found both numerically and analytically[12,13]. In contrast to the standard squeezed state generation in non-equilibrium situations, quantum squeezing at the SRPT critical point is intrinsically stable and resilient against any noise even at finite temperatures[13]. As a result of this stable squeezing, such systems are intrinsically robust against decoherence, which is especially important for quantum sensing and continuous-variable quantum information technology.

A unique aspect of the SRPT is its manifestation as a physical phenomenon associated with the thermal-equilibrium state of a coupled light–matter system. This deviates from typical quantum-optics research that mainly deals with non-equilibrium excited-state dynamics. The occurrence of non-equilibrium SRPTs has been demonstrated in cold-atom systems driven by laser beams[14–17]. Although the temperature of cold atoms in a steady state is usually measured by the variance of their kinetic energy, the non-equilibrium SRPTs are inherently driven, dissipative, and transient phenomena. Effective temperatures defined with the driving power in the non-equilibrium SRPTs have been discussed theoretically[17]. However, the realization of SRPTs under pure thermal equilibrium is yet to be achieved. The existence of a SRPT analogue has been theoretically proposed for a superconducting circuit maintained under thermal equilibrium[18–24], but no experimental observations of this effect have been reported.

The present work shows theoretically that the phase transition in erbium orthoferrite ($ErFeO_3$) with a critical temperature T_c of ~4 K, known as the low-temperature phase transition (LTPT), is a magnonic SRPT, that is, an SRPT in which the Er^{3+} spins cooperatively couple with the Fe^{3+} magnonic field (spin-wave field) instead of with a photonic field as in the originally proposed SRPT. Specifically, we found that the LTPT occurs owing to Er^{3+}–magnon coupling, even in the absence of direct Er^{3+}–Er^{3+} exchange interactions. In addition, we observed that the Er^{3+}–magnon coupling enhances the T_c value for LTPT compared to that obtained via direct Er^{3+}–Er^{3+} interactions. These results demonstrate the uniqueness of $ErFeO_3$ as a physical system in which SRPT can be experimentally realized under thermal equilibrium.

Results

Principle of magnonic SRPT. The SRPT was first suggested in 1973 by Hepp and Lieb[1], and has been extensively discussed based on the Dicke model[6], conventionally expressed as

$$\frac{\hat{\mathcal{H}}_{Dicke}}{\hbar} \equiv \omega_{ph}\hat{a}^\dagger\hat{a} + \omega_{ex}\hat{S}_x + \frac{i2g}{\sqrt{N}}(\hat{a}^\dagger - \hat{a})\hat{S}_z. \qquad (1)$$

Here, $\hat{a}$ is the annihilation operator of a photon in a photonic mode with resonance frequency ω_{ph}, $\hat{S}_{x,y,z}$ are spin $\frac{N}{2}$ operators representing an ensemble of two-level atoms with a transition frequency ω_{ex}, and N is the number of atoms. The last term

represents the coupling between the photonic mode and atomic ensemble with strength g. In the thermodynamic limit, i.e., in the limit of $N \to \infty$, the SRPT arises when $4g^2 > \omega_{ph}\omega_{ex}$, i.e., in the ultrastrong coupling regime $g \gtrsim \omega_{ph}, \omega_{ex}$[3–5]. Below T_c, the expectation values of the photon annihilation operator $\langle\hat{a}\rangle$ and spin operator $\langle\hat{S}_z\rangle$ become non-zero, indicating the spontaneous appearance of a static electromagnetic field and static polarization (or a persistent electric current) in thermal equilibrium.

The magnonic SRPT is a phase transition caused by ultrastrong coupling between a magnonic mode and other collective excitations in matter. The spontaneous appearance of magnons, also known as spin waves, reflects the spontaneous ordering of a spin ensemble mediating them in a certain direction. We present an explanation of the magnonic SRPT in the case of $ErFeO_3$ below.

Each unit cell in $ErFeO_3$ contains four Er^{3+} ions and four Fe^{3+} ions. The four Fe^{3+} spins, each of which has an angular momentum of $\hbar S = (5/2)\hbar$, are oriented in different directions, even in the absence of an external direct current (DC) magnetic field[25]. However, it is known that the Fe^{3+} spin resonances (magnon modes) may be described well by considering only two spins $\hat{\mathbf{S}}^{A/B}$ comprising two real Fe^{3+} spins, which are usually treated as a single spin with $S = 5/2$. In such a two-sublattice model of Fe^{3+}, as depicted in Fig. 1a, the two spins $\hat{\mathbf{S}}^{A/B}$ are ordered antiferromagnetically along the c axis at $T_c < T \lesssim 90$ K, but are slightly canted toward the a axis and show weak magnetization (the Fe^{3+} spins exhibit the so-called spin-reorientation transition at 90 K $\lesssim T \lesssim 100$ K[26–28]). In contrast, the Er^{3+} spins are paramagnetic at $T > T_c$, and they are directed along the a axis by the weak Fe^{3+} magnetization. This phase is called the Γ_2 phase[29].

At $T < T_c$, as shown in Fig. 1b, when a two-sublattice model is used for the Er^{3+} spins, they are ordered antiferromagnetically along the c axis, with a canting toward the a axis due to the Fe^{3+} magnetization. Simultaneously, the Fe^{3+} antiferromagnetism (AFM) vector $\mathbf{S}^A - \mathbf{S}^B$ rotates gradually in the bc plane. The rotation angle measured from the c axis, φ, was estimated to be $49°$ at $T = 0$ K[29]. This low-temperature phase is called the Γ_{12} phase[29].

The second-order phase transition between phases Γ_2 and Γ_{12} at $T_c \sim 4$ K is called the LTPT[27,28]. There are at least two contributions to the LTPT, namely the Er^{3+}–Er^{3+} and Er^{3+}–Fe^{3+} exchange interactions[29,30]. Although the former is usually stronger
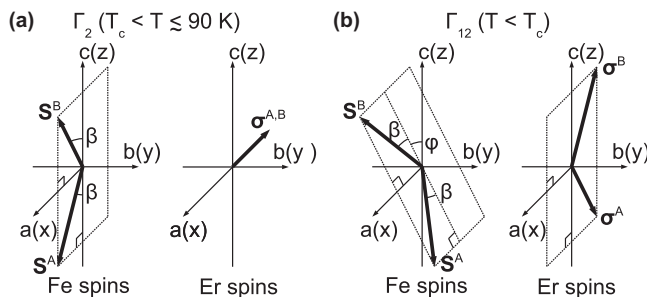

Fig. 1 Spin configurations in $ErFeO_3$ below and above T_c ~ 4 K. In this study, we considered two-sublattice models both for Er^{3+} and Fe^{3+} spins. **a** In the high-temperature ($T_c < T \lesssim 90$ K, Γ_2) phase, the Fe^{3+} spins are ordered antiferromagnetically along the c axis with a slight canting toward the a axis. The Er^{3+} spins are paramagnetic and directed toward the a axis by the weak Fe^{3+} magnetization. **b** In the low-temperature ($T < T_c$, Γ_{12}) phase, the Er^{3+} spins are ordered antiferromagnetically along the c axis, and the antiferromagnetic (AFM) vector $\mathbf{S}^A - \mathbf{S}^B$ of the Fe^{3+} spins rotates in the bc plane.

than the latter and is largely responsible for LTPT, the latter is essential for explaining the rotation of the Fe^{3+} AFM vector.

In the absence of the Er^{3+}–Fe^{3+} exchange interactions, as shown in Fig. 1a, the Fe^{3+} spins are ordered antiferromagnetically along the c axis with a slight canting toward the a axis in the ground state of the Fe^{3+} subsystem. Considering that the magnon excitation in this Fe^{3+} subsystem corresponds to the photon excitation in the electromagnetic vacuum, the rotation of the Fe^{3+} AFM vector (at $T < T_c$ as shown in Fig. 1b) indicates the spontaneous appearance of magnons, corresponding to the appearance of photons (a static electromagnetic field) in the ordinary SRPT, in thermal equilibrium. The ordering of the Er^{3+} spins corresponds to the spontaneous appearance of an atomic field (polarization) in the SRPT.

Owing to the phenomenological similarities between the LTPT and SRPT, the microscopic models governing these phase transitions may be considered transferable. This constitutes the basic concept of magnonic SRPT proposed in this study.

ErFeO$_3$ spin model. First, we describe a general spin model for $Er_xY_{1-x}FeO_3$ ($0 \le x \le 1$), which is consistent with our previous experimental study[31]. The replacement of Er^{3+} ions with non-magnetic Y^{3+} ions simply reduces the density of the rare-earth (Er^{3+}) spins without changing the crystal structure or magnetic configuration of Fe^{3+} spins in the Γ_2 phase[31,32]. Although the present work largely uses $x = 1$ ($ErFeO_3$), the x-dependence is considered in "Spin resonance frequencies" in Supplementary Methods.

The Hamiltonian for the spins in $Er_xY_{1-x}FeO_3$ consists of three parts, i.e.,

$$\mathcal{H} = \mathcal{H}_{Fe} + \mathcal{H}_{Er} + \mathcal{H}_{Er-Fe}, \tag{2}$$

where $\mathcal{H}_{Fe}$, $\mathcal{H}_{Er}$, and $\mathcal{H}_{Er-Fe}$ are the Hamiltonians of the Fe^{3+} spins, Er^{3+} spins, and Er^{3+}–Fe^{3+} interactions, respectively.

As explained above, we employ the two-sublattice model for the Fe^{3+} spins following Herrmann's model[33] and the methods of our prior works[31–34]. The Hamiltonian of the Fe^{3+} spins is

$$\hat{\mathcal{H}}_{Fe} = \sum_{s=A,B} \sum_{i=1}^{N_0} \mu_B \hat{S}_i^s \cdot \mathfrak{g}^{Fe} \cdot \mathbf{B}^{DC} + J_{Fe} \sum_{n.n} \hat{S}_i^A \cdot \hat{S}_{i'}^B$$
$$- D_y^{Fe} \sum_{n.n.} \left(\hat{S}_{i,z}^A \hat{S}_{i',x}^B - \hat{S}_{i',z}^B \hat{S}_{i,x}^A \right)$$
$$- \sum_{i=1}^{N_0} \left(A_x \hat{S}_{i,x}^{A}{}^2 + A_z \hat{S}_{i,z}^{A}{}^2 + A_{xz} \hat{S}_{i,x}^A \hat{S}_{i,z}^A \right)$$
$$- \sum_{i=1}^{N_0} \left(A_x \hat{S}_{i,x}^{B}{}^2 + A_z \hat{S}_{i,z}^{B}{}^2 - A_{xz} \hat{S}_{i,x}^B \hat{S}_{i,z}^B \right). \tag{3}$$

Here, $\hat{S}_i^{A/B}$ is the operator of the Fe^{3+} spin $S = 5/2$ at the i-th site in the A/B sublattice, while $\sum_{n.n.}$ represents a summation over all nearest-neighbor couplings. The number of nearest neighbors is

$$z_{Fe} = 6. \tag{4}$$

N_0 denotes the number of Fe^{3+} spins in each sublattice and is equal to the unit cell count in $ErFeO_3$. A total of $2N_0$ spins represent the Fe^{3+} subsystem. μ_B is the Bohr magneton, and

$$\mathfrak{g}^{Fe} \equiv \begin{pmatrix} \mathfrak{g}_x^{Fe} & 0 & 0 \\ 0 & \mathfrak{g}_y^{Fe} & 0 \\ 0 & 0 & \mathfrak{g}_z^{Fe} \end{pmatrix} \tag{5}$$

is the g-factor tensor of the Fe^{3+} spins. In the following, the g-factor of free electron spin is expressed as $\mathfrak{g}$. $\mathbf{B}^{DC}$ is the external

DC magnetic flux density. J_{Fe} and D_y^{Fe} are the strengths of the isotropic and Dzyaloshinkii–Moriya-type exchange interaction strengths between the Fe^{3+} spins, respectively. A_x, A_z, and A_{xz} are the energies expressing the magnetic anisotropy of the Fe^{3+} spins.

Although we expressed the Er^{3+} subsystem using a single spin lattice for the paramagnetic Er^{3+} spins ($T > T_c$) in our previous works[31,34], in this study we employ a two-sublattice model for the Er^{3+} spins to describe the Er^{3+}–Er^{3+} exchange interaction and LTPT. The Hamiltonian of the Er^{3+} spins is

$$\hat{\mathcal{H}}_{Er} = - \sum_{s=A,B} \sum_{i=1}^{N_0} \hat{\mu}_i^s \cdot \mathbf{B}^{DC} + J_{Er} \sum_{n.n.} \hat{R}_i^A \cdot \hat{R}_{i'}^B. \tag{6}$$

Here, $\hat{R}_i^{A/B}$ is the operator of rare-earth (Er^{3+} or Y^{3+}) spin at the site i in the A/B sublattice. For $Er_xY_{1-x}FeO_3$, the rare-earth spins are represented randomly as $s = A, B$; i.e.,

$$\hat{R}_i^s = \begin{cases} \hat{\sigma}_i^s & \text{for } Er^{3+} \\ 0 & \text{for } Y^{3+} \end{cases}. \tag{7}$$

We describe each Er^{3+} spin using a vector of Pauli operators $\hat{\sigma}_i^s \equiv (\hat{\sigma}_{i,x}^s, \hat{\sigma}_{i,y}^s, \hat{\sigma}_{i,z}^s)^t$ satisfying $\hat{\sigma}_{i,\xi}^s \hat{\sigma}_{i,\xi}^s = 1$, $[\hat{\sigma}_{i,\xi}^s, \hat{\sigma}_{i',\xi}^{s'}] = 0$ ($\xi = x, y, z$), $[\hat{\sigma}_{i,x}^s, \hat{\sigma}_{i',y}^{s'}] = i2\hat{\sigma}_{i,z}^s \delta_{s,s'} \delta_{i,i'}$, $[\hat{\sigma}_{i,y}^s, \hat{\sigma}_{i',z}^{s'}] = i2\hat{\sigma}_{i,x}^s \delta_{s,s'} \delta_{i,i'}$, and $[\hat{\sigma}_{i,z}^s, \hat{\sigma}_{i',x}^{s'}] = i2\hat{\sigma}_{i,y}^s \delta_{s,s'} \delta_{i,i'}$, where $\delta_{i,j}$ is the Kronecker delta. The Y^{3+} ion is non-magnetic, and $\hat{R}_i^s$ is replaced with 0. The first term in Eq. (6) represents the Zeeman effect, and the magnetic moment is expressed in terms of the anisotropic g factors $\mathfrak{g}_{x,y,z}^{Er}$ for the Er^{3+} spins as

$$\hat{\mu}_i^s \equiv -\frac{1}{2}\mu_B (\mathfrak{g}_x^{Er} \hat{R}_{i,x}^s, \mathfrak{g}_y^{Er} \hat{R}_{i,y}^s, \mathfrak{g}_z^{Er} \hat{R}_{i,z}^s)^t = -\frac{1}{2}\mu_B \mathfrak{g}^{Er} \cdot \hat{R}_i^s. \tag{8}$$

The factor $1/2$ is added because $(1/2)\hat{\sigma}_i^s$ theoretically corresponds to a spin $\frac{1}{2}$ operator. We define the g-factor tensor for the Er^{3+} spins as

$$\mathfrak{g}^{Er} \equiv \begin{pmatrix} \mathfrak{g}_x^{Er} & 0 & 0 \\ 0 & \mathfrak{g}_y^{Er} & 0 \\ 0 & 0 & \mathfrak{g}_z^{Er} \end{pmatrix}. \tag{9}$$

The second term in Eq. (6) represents the $Er^{3+} - Er^{3+}$ exchange interaction with strength J_{Er}. Because the Er^{3+} ions are diluted in $Er_xY_{1-x}FeO_3$, the number of nearest-neighbor Er^{3+} spins is effectively given by

$$z_{Er} = 6x. \tag{10}$$

We describe the Er^{3+}–Fe^{3+} exchange interactions as

$$\hat{\mathcal{H}}_{Er-Fe} = \sum_{i=1}^{N_0} \sum_{s,s'=A,B} \left[J\hat{R}_i^s \cdot \hat{S}_i^{s'} + \mathbf{D}^{s,s'} \cdot (\hat{R}_i^s \times \hat{S}_i^{s'}) \right]. \tag{11}$$

In our model, the Er^{3+}–Fe^{3+} interaction is closed in each unit cell; that is, the Er^{3+} and Fe^{3+} spins in the same unit cell interact with each other but do not interact with the spins in other unit cells. J and $\mathbf{D}^{s,s'}$ are the strengths of the isotropic and antisymmetric exchange interactions, respectively[31–34]. Considering the spin configuration at $T < T_c$ with no external DC magnetic field (see more details in "Reduction of number of parameters" in Supplementary Methods), we assume that $\mathbf{D}^{s,s'}$ are expressed in terms of two values D_x and D_y as

$$\mathbf{D}^{A,A} = (D_x, D_y, 0)^t, \tag{12}$$

$$\mathbf{D}^{A,B} = (-D_x, -D_y, 0)^t, \tag{13}$$
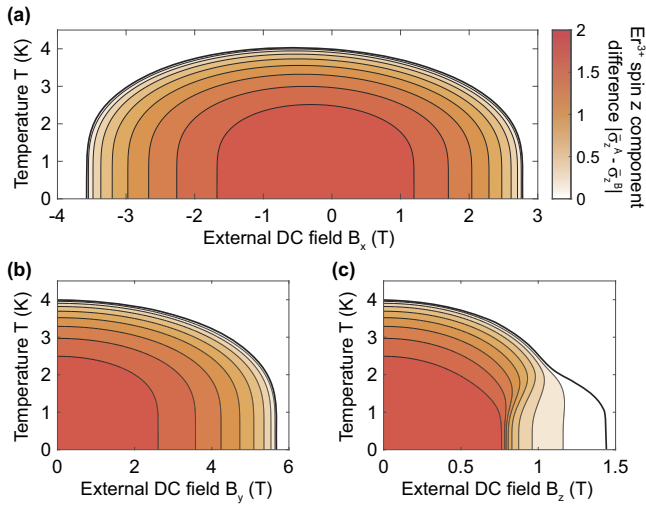
$$\mathbf{D}^{B,A} = (-D_x, D_y, 0)^t, \tag{14}$$

Fig. 2 Phase diagrams of spins in ErFeO$_3$ calculated using the mean-field method. An external DC magnetic field was applied along the **a** a. **b** b. **c** c axes. The difference $|\bar{\sigma}_z^A - \bar{\sigma}_z^B|$ of the z components of the thermal-equilibrium values of Er^{3+} spins is mapped in red. The bold solid curves represent the phase boundaries. The external direct current (DC) magnetic field was varied from zero to positive or negative values at a fixed temperature. As ErFeO$_3$ shows weak magnetization along the a axis, the critical field depends on whether the field is parallel or antiparallel to the magnetization in Fig. 2a.

$$\mathbf{D}^{B,B} = (D_x, -D_y, 0)^t. \tag{15}$$

As explained in detail in the section "Mean-field Calculation Method" we assume that the y components $\hat{R}_{i,y}^{A/B}$ of the Er^{3+} spins are not influenced by the Er^{3+}–Fe^{3+} interactions by implicitly considering a higher energy potential than that of the Er^{3+}–Fe^{3+} interaction strengths J and $\mathbf{D}^{s,s'}$ along the b axis. This assumption helps to obtain an appropriate description of LTPT in accordance with our numerical calculations.

The actual values of the parameters appearing in our proposed spin model are provided in "Parameters" together with a description of how they were determined based on recent experimental results of terahertz magnetospectroscopy[31] and magnetization measurements[26].

LTPT phase diagrams. Next, we show that our spin model certainly describes the thermal equilibrium (average) values of the Er^{3+} spins $\bar{\sigma}^{A/B}$ and Fe^{3+} spins $\bar{\mathbf{S}}^{A/B}$ in the zero-wavenumber (infinite-wavelength) limit using the mean-field method. Details pertaining to the mean-field method are provided in the section "Mean-field Calculation Method." Because we simply considered a homogeneous external DC magnetic flux density $\mathbf{B}^{DC}$, $\bar{\sigma}^{A/B}$ and $\bar{\mathbf{S}}^{A/B}$ were independent of the site index i.

Figure 2a–c show the calculated phase diagrams as functions of T and $\mathbf{B}^{DC}$, applied along the a, b, and c axes, respectively. The difference $|\bar{\sigma}_z^A - \bar{\sigma}_z^B|$ in the z components of the thermal equilibrium values of Er^{3+} spins (AFM vector) is plotted in red. $|\bar{\sigma}_z^A - \bar{\sigma}_z^B|$ is the order parameter for the LTPT in the presence of an external DC magnetic field in general, although the rotation angle of the Fe^{3+} AFM vector can be utilized as an alternative order parameter if the external DC field is zero or is along the a axis. The bold solid curves represent phase boundaries.
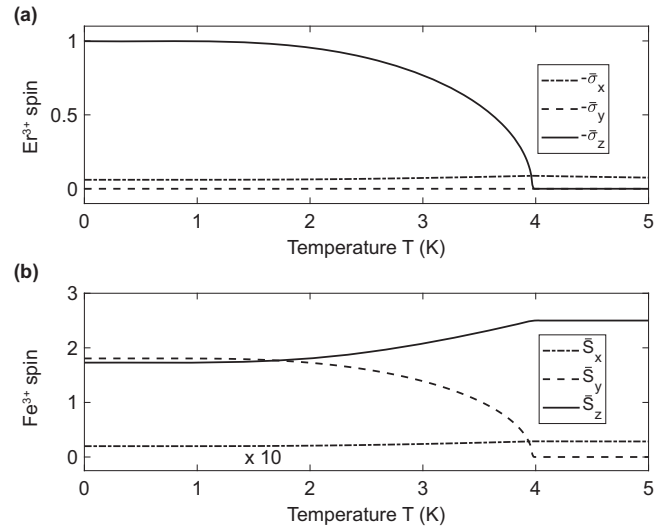

Fig. 3 Thermal equilibrium spin values. a Er^{3+} spin. **b** Fe^{3+} spin calculated using the mean-field method as functions of T in the case of zero external direct current (DC) magnetic field. As shown in Fig. 3a, $\bar{\sigma}_z = \bar{\sigma}_z^A = -\bar{\sigma}_z^B$ spontaneously appears below $T_c = 4.0$ K, i.e., the Er^{3+} spins are antiferromagnetically ordered along the c axis. They show magnetization along the a axis as $\bar{\sigma}_x = \bar{\sigma}_x^{A/B}$ due to the Er^{3+}–Fe^{3+} exchange interaction with the weak Fe^{3+} magnetization along the a axis, whereas $\bar{\sigma}_y = \bar{\sigma}_y^{A/B} = 0$. As shown in Fig. 3b, above T_c, the Fe^{3+} spins are ordered antiferromagnetically along the c axis as $\bar{S}_z = -\bar{S}_z^A = \bar{S}_z^B$, whereas they are slightly canted toward the a axis as $\bar{S}_x = \bar{S}_x^{A/B}$, and $\bar{S}_y = \bar{S}_y^A = -\bar{S}_y^B = 0$. Below T_c, the Fe^{3+} spins rotate in the bc plane, and the rotation angle is $\varphi = \arctan(\bar{S}_y/\bar{S}_z) = 46°$ at $T = 0$ K with our parameters.

These phase diagrams are consistent with those reported by Zhang et al.[26]. As shown in Fig. 2a, because ErFeO$_3$ possesses a weak magnetization along the a axis, the critical field depends on whether the field is parallel (in the same direction) or antiparallel (in the opposite direction) to the magnetization. The parameters used in the calculations are provided in "Parameters."

Figure 3 plots the thermal equilibrium values of the Er^{3+} and Fe^{3+} spins in the absence of an external DC magnetic field as functions of temperature. The LTPT, that is, the antiferromagnetic ordering of the Er^{3+} spins along the c axis and the rotation of the Fe^{3+} spins in the bc plane[29], are reproduced well in our spin model. The rotation angle of the Fe^{3+} AFM vector is $\varphi = 46°$ at $T = 0$ K with our parameters. This value is approximately equal to the experimentally estimated value $\varphi = 49°$ [29].

Extended Dicke Hamiltonian. The mean-field method employed in this study, as illustrated in Figs. 2 and 3, is a standard means of analysing magnetic phase transitions. To investigate the analogy between LTPT and SRPT using the Dicke model, we derive an extended version of the Dicke model transformed from the spin model in Eq. (2). This derivation is given in detail in the section "Derivation of Extended Dicke Hamiltonian".

The extended Dicke Hamiltonian minimally including the terms relevant to the LTPT in an external DC magnetic field applied along the a axis, where the Γ_{12} symmetry remains, is

$$\hat{\mathcal{H}}/\hbar \approx \omega_\pi \hat{a}_\pi^\dagger \hat{a}_\pi + \omega_{Er} \hat{\Sigma}_z + \frac{2z_{Er}J_{Er}}{N\hbar}\left(\hat{\Sigma}_x^2 - \hat{\Sigma}_z^2\right)$$

$$+ \frac{2g_x}{\sqrt{N}}(\hat{a}_\pi^\dagger + \hat{a}_\pi)\hat{\Sigma}_x + \frac{i2g_z}{\sqrt{N}}(\hat{a}_\pi^\dagger - \hat{a}_\pi)\hat{\Sigma}_z. \tag{16}$$

Here, $\hat{a}_\pi$ $(\hat{a}_\pi^\dagger)$ is the annihilation (creation) operator of an Fe^{3+} magnon in the quasi-antiferromagnetic (qAFM) mode[33]. The eigenfrequency $\omega_\pi = 2\pi \times 0.896$ THz can be evaluated using Eq. (63). The actual value was evaluated using the parameters shown in "Parameters." The Er^{3+} resonance frequency is defined as follows.

$$\omega_{Er} \equiv \frac{|E_x + \mathfrak{g}_x^{Er} \mu_B B_x^{DC}|}{\hbar}. \tag{17}$$

$$E_x \equiv 4S(J \sin \beta_0 + D_y \cos \beta_0) = h \times 0.023 \text{ THz}. \tag{18}$$

The total number of $\frac{1}{2}$ spins (Er^{3+} spins) in the two sublattices is

$$N \equiv 2xN_0. \tag{19}$$

$\hat{\Sigma}_{x,y,z}$ are spin $\frac{N}{2}$ operators representing the rare-earth spins (a detailed definition is given in Eq. (92)). The two Er^{3+}–magnon coupling strengths in the last two terms of Eq. (16) are defined as follows.

$$\hbar g_x = \sqrt{2xS}(J \cos \beta_0 - D_y \sin \beta_0)\left(\frac{b+a}{d-c}\right)^{1/4} = h \times \sqrt{x} \times 0.051 \text{ THz}, \tag{20}$$

$$\hbar g_z = \sqrt{2xS} D_x \left(\frac{d-c}{b+a}\right)^{1/4} = h \times \sqrt{x} \times 0.116 \text{ THz}. \tag{21}$$

Comparing Eq. (16) with Eq. (1) (the Dicke model), because $\hat{a}_\pi$ and $\hat{\Sigma}_{x,y,z}$ in Eq. (16) correspond to $\hat{a}$ and $\hat{S}_{x,y,z}$ in Eq. (1), respectively, we may observe that the g_z term in Eq. (16) corresponds to the matter–photon coupling (transverse coupling), that is, the last term in Eq. (1). In addition, the g_x term represents longitudinal coupling, and the term J_{Er} describes the Er^{3+}–Er^{3+} exchange interactions in Eq. (16). The coupling strength $g_z = 2\pi \times 0.116$ THz shows the system fall into the ultrastrong regime because it is a considerable fraction of the Er^{3+} resonance and qAFM magnon frequencies, $E_x = h \times 0.023$ THz and $\omega_\pi = 2\pi \times 0.896$ THz. When the g_z term causes an SRPT, $\langle \hat{\Sigma}_z \rangle$ spontaneously acquires a non-zero value in thermal equilibrium, corresponding to the antiferromagnetic ordering of the Er^{3+} spins along the c axis. As explained in "Derivation of Extended Dicke Hamiltonian," the spontaneous appearance of non-zero $\langle i(\hat{a}_\pi^\dagger - \hat{a}_\pi)\rangle$ coupled with $\hat{\Sigma}_z$ in the g_z term, corresponds to that of the Fe^{3+} AFM vector in the b axis and causes its rotation in the bc plane. The Fe^{3+} quasi-ferromagnetic (qFM) magnon mode can be neglected in describing the LTPT, because the AFM ordering of the Er^{3+} spins and the spontaneous appearance of qAFM magnons are rather favoured and they prevent the appearance of qFM magnons, which feel additional energy cost under the ordering of the Er^{3+} spins and the qAFM magnons.

As seen in Eqs. (20) and (21), the transverse coupling strength g_z depends on D_x, and the longitudinal coupling strength g_x depends on J and D_y. These expressions are reasonable from the perspective of the spin model in Eq. (11). The D_x antisymmetric Er^{3+}–Fe^{3+} exchange interaction is essential for the LTPT because it couples $\hat{\sigma}_z^{A/B}$ and $\hat{S}_y^{A/B}$, which appear spontaneously at $T < T_c$. In contrast, the J and D_y exchange interactions are not directly related to the LTPT because these interaction terms do not couple $\hat{\sigma}_z^{A/B}$ and $\hat{S}_y^{A/B}$ directly.

Evidence of magnonic SRPT. Using the semiclassical method described in "Semiclassical Calculation Method" with the extended Dicke Hamiltonian in Eq. (16), we calculated the thermal
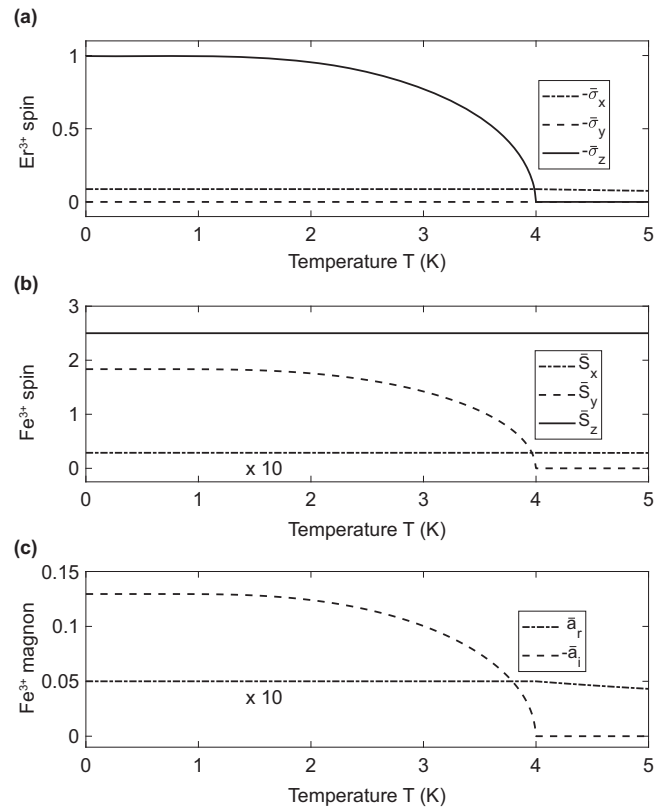

Fig. 4 Thermal equilibrium spin and amplitude values. a Er^{3+} spins. **b** Fe^{3+} spins. **c** Fe^{3+} magnon amplitudes as functions of T. These values were calculated using the semiclassical method with the extended Dicke Hamiltonian in the case of zero external direct current (DC) magnetic field. Figure 4a, b are nearly the same as Fig. 3a, b, respectively, except $\bar{S}_z$, which changes only slightly due to magnon bosonization. The Fe^{3+} spins, $\bar{S}_{x,y,z}$, were calculated using Eqs. (113)–(115) with the thermal equilibrium value of the quasi-antiferromagnetic (qAFM) magnon annihilation operator $\langle \hat{a}_\pi \rangle = \sqrt{N}(\bar{a}_r + i\bar{a}_i)$ plotted in Fig. 4c.

equilibrium values of the Er^{3+} and Fe^{3+} spins and magnon amplitudes as functions of temperature. Here and also in the calculation of the LTPT phase diagrams by the mean-field approach, we implicitly assumed that a thermal bath is connected to the extended Dicke Hamiltonian in Eq. (16) [and the spin model in Eq. (2)]. The thermal bath simply ensures that the system is in thermal equilibrium at a certain temperature in the present calculations, whereas it causes the energy loss and decoherence in non-equilibrium dynamics of Er^{3+} spins and Fe^{3+} magnons.

Figure 4a–c show the thermal equilibrium values of the Er^{3+} spins $\bar{\sigma}_{x,y,z} = \langle \hat{\Sigma}_{x,y,z} \rangle / (N/2)$, Fe^{3+} spins $\bar{S}_{x,y,z}$, and Fe^{3+} qAFM magnons $\bar{a}_{r,i}$ as functions of temperature in the absence of an external DC magnetic field, i.e., with $\mathbf{B}^{DC} = 0$. $\bar{S}_{x,y,z}$ were calculated using Eqs. (113)–(115) with $\langle \hat{a}_\pi \rangle = \sqrt{N}(\bar{a}_r + i\bar{a}_i)$. Figure 4a, b, respectively, reproduce Fig. 3a, b calculated using the mean-field method with the original spin model, including T_c, although $\bar{S}_z$ differs. As depicted in Fig. 3b, a decrease in temperature causes a reduction in $\bar{S}_z$ along with the spontaneous appearance of $\bar{S}_y$, whereas Fig. 4b reveals $\bar{S}_z$ to remain nearly constant. This difference exists because $\bar{S}_x^2 + \bar{S}_y^2 + \bar{S}_z^2 = S^2$ does not hold in the extended Dicke Hamiltonian derived via magnon quantization (i.e., bosonisation of Fe^{3+} spin modulations). The
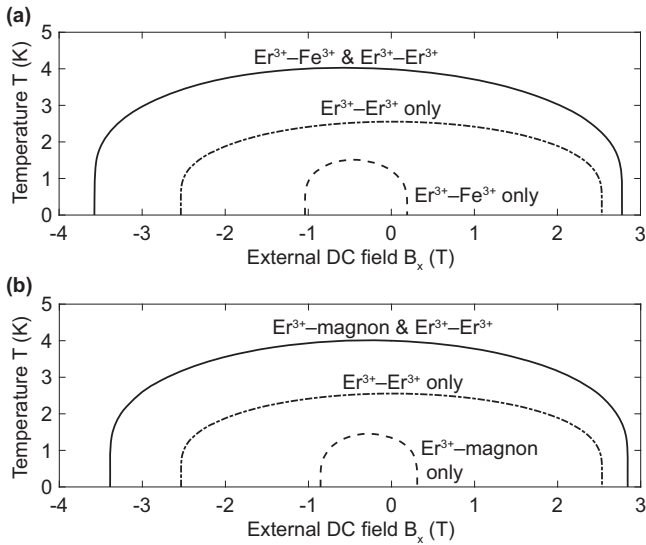
(a)

(b)

Fig. 5 Phase boundaries of the low-temperature phase transition (LTPT) in ErFeO₃. Boundaries calculated using the (**a**) mean-field method and (**b**) semiclassical method with the extended Dicke Hamiltonian. An external direct current (DC) magnetic field is applied along the a axis. The solid curves are the phase boundaries determined using the full Hamiltonian, and those in Figs. 5a and 2a are equivalent. The dashed-dotted curves are the phase boundaries in the absence of Er^{3+}–magnon coupling (Er^{3+}–Fe^{3+} exchange interactions). The dashed curves are those obtained in the absence of Er^{3+}–Er^{3+} exchange interactions, i.e., the LTPT can be caused solely by the Er^{3+}–magnon coupling and thus can be interpreted as a magnonic superradiant phase transition (SRPT).

ultrastrong term g_z, the last term in Eq. (16), causes the spontaneous appearance of $\bar{\sigma}_z$ and $\bar{a}_i$, as shown in Fig. 4a, c, respectively, and the latter causes a non-zero $\bar{S}_y$ through Eq. (114). The Fe^{3+} AFM vector is rotated due to the spontaneous appearance of a non-zero $\bar{S}_y$ when $\bar{S}_x^2 + \bar{S}_y^2 + \bar{S}_z^2 = S^2$ holds. Thus, the LTPT, that is, the spontaneous ordering of Er^{3+} spins (spontaneous appearance of $\bar{\sigma}_z$) and the spontaneous rotation of Fe^{3+} AFM vector (spontaneous appearance of $\bar{a}_i$ and $\bar{S}_y$), is caused by the Er^{3+}–magnon coupling.

To compare the contributions of the Er^{3+}–magnon couplings and Er^{3+}–Er^{3+} exchange interactions for the LTPT, Fig. 5 depicts the phase boundaries calculated using the full Hamiltonian (solid curves) as well as in the absence of Er^{3+}–Fe^{3+} exchange interactions (dashed–dotted curve; $J = D_x = D_y = g_z = g_x = 0$) and Er^{3+}–Er^{3+} exchange interactions (dashed curve; $J_{Er} = 0$). Figure 5a, b illustrate the results obtained using the mean-field and semiclassical methods with extended Dicke Hamiltonian, respectively. The solid curve in Fig. 5a is equal to that in Fig. 2a. The slight differences between Fig. 5a, b are discussed in "Aspects of phase boundaries" in Supplementary Methods.

The dashed curves ($J_{Er} = 0$) in Fig. 5 reveal that the phase transition occurs even in the absence of Er^{3+}–Er^{3+} exchange interactions and that T_c equals approximately 1.2 K at $\mathbf{B}^{DC} = \mathbf{0}$. Thus, Er^{3+}–magnon coupling alone can cause the LTPT. In this sense, the LTPT can be interpreted as a magnonic SRPT because the Er^{3+}–magnon coupling is sufficiently strong for the phase transition to occur.

On the other hand, in the absence of Er^{3+}–magnon coupling, as denoted by the dashed–dotted curves, T_c is approximately 2.6 K at $\mathbf{B}^{DC} = \mathbf{0}$. This result appears to indicate that the contribution of the Er^{3+}–Er^{3+} exchange interactions is larger than that of the Er^{3+}–magnon coupling. However, the actual T_c is

4 K; that is, the Er^{3+}–magnon coupling enhances the T_c of the phase transition. In the same manner, the critical magnetic fields are also enhanced. These facts are similar to the suggestion of T_c enhancement through photon–matter coupling by Mazza and Georges[35]; however, in their case, phase transition does not occur solely by photon–matter coupling, and their model does not guarantee gauge invariance[36,37].

Although the g_z term causes the spontaneous appearance of both $\bar{\sigma}_z$ and $\bar{S}_y$ following the above-mentioned description of the SRPT, a non-zero $\bar{\sigma}_z$ can also spontaneously appear due to the J_{Er} term (Er^{3+}–Er^{3+} exchange interactions). Although Er^{3+}–magnon coupling is inevitable for the spontaneous rotation of the Fe^{3+} AFM vector (spontaneous appearance of $\bar{S}_y$), we quantitatively evaluate the contributions of the Er^{3+}–magnon coupling and Er^{3+}–Er^{3+} exchange interactions for the LTPT as follows.

The two contributions to the LTPT can be determined by analysing the condition for the SRPT in our extended Dicke Hamiltonian in Eq. (16) under the Holstein–Primakoff transformation[38–40]. The detailed calculations are discussed in the "Condition for SRPT in Extended Dicke Hamiltonian" section. The condition can finally be expressed as

$$\frac{4g_z^2}{\omega_\pi \omega_{Er}} - \frac{4g_x^2}{\omega_\pi \omega_{Er}} + \frac{4z_{Er} J_{Er}}{\hbar \omega_{Er}} > 1. \quad (22)$$

For $J_{Er} = g_x = 0$, this expression is reduced to $4g_z^2 > \omega_\pi \omega_{Er}$ for the SRPT in the Dicke model, Eq. (1).

The three terms on the left-hand side of Eq. (22) are evaluated as follows.

$$D_{g_z} \equiv 4g_z^2/(\omega_\pi \omega_{Er}) = 2.65, \quad (23)$$

$$D_{g_x} \equiv -4g_x^2/(\omega_\pi \omega_{Er}) = -0.51, \quad (24)$$

$$D_{J_{Er}} \equiv 4z_{Er} J_{Er}/(\hbar \omega_{Er}) = 9.29. \quad (25)$$

In the following, we refer to these quantities as *coupling depths*. They are dimensionless measures of coupling strength and are determined based on the appearance of the SRPT. As seen in Eq. (22), the SRPT occurs when the sum of these coupling depths exceeds unity, i.e., $D_{g_z} + D_{g_x} + D_{J_{Er}} > 1$. The coupling depth $D_{J_{Er}}$ of the J_{Er} term is the largest, which is consistent with Fig. 5. The g_x term (longitudinal coupling) has a negative contribution to the SRPT ($D_{g_x} < 0$). Among the three couplings, the contribution of the g_z term is $D_{g_z}/(D_{g_z} + D_{g_x} + D_{J_{Er}}) = 0.23$, and that of the total Er^{3+}–magnon coupling is $(D_{g_z} + D_{g_x})/(D_{g_z} + D_{g_x} + D_{J_{Er}}) = 0.19$. These values are roughly equal to $1.3\,K/(1.3\,K + 3.4\,K) = 0.28$, as estimated by Kadomtseva et al.[29] However, the longitudinal coupling (g_x term) was not included in their model[41,42], and the parameters were determined only by the phase boundary for $\mathbf{B}^{DC}//a$.

Considering the analogy between an LTPT and SRPT, the coupling depth of the g_z term satisfies $D_{g_z} > 1$ and $D_{g_z} + D_{g_x} > 1$. This result suggests that the transverse Er^{3+}–magnon coupling is much stronger than the longitudinal coupling (giving a negative contribution) and is sufficiently strong to cause the SRPT alone. In this sense, we can conclude that the LTPT in ErFeO₃ is a magnonic SRPT obtained in the extended Dicke Hamiltonian with direct atom–atom interaction and longitudinal coupling (g_x term).

Discussion

As shown above, we quantitatively confirmed that the LTPT in ErFeO₃ is a magnonic version of the SRPT in thermal

equilibrium. This is the first confirmation of the SRPT since its proposal in 1973[1].

Early reports on the SRPT suggested its no-go theorems[43–46], implying that thermal-equilibrium SRPTs cannot be realized in systems described by the minimal-coupling Hamiltonian, that is, charged particles (without spins) interacting with electromagnetic fields. Because the classical treatment of the electromagnetic fields used in proofs of such no-go theorems can be justified only in limited situations[2,45–49], proposals of counter-examples against the no-go theorems and criticisms against the counter-examples have been repeated in SRPT research[35–37,50–57].

One means of evading the no-go theorems involves introducing another degree of freedom, such as spin[44]. For example, it has been shown that the Rashba spin–orbit coupling can cause paramagnetic instability in an ultrastrongly coupled system between a cyclotron resonance and cavity photon field, implying an SRPT[37]. Further, it has been pointed out recently[37,58,59] that the coupling between matter and a spatially-varying multi-mode cavity fields plays a key role for circumventing the no-go theorem. Another method is to utilize various types of interactions and spin waves in magnetic materials, which cannot be described by the minimal-coupling Hamiltonian.

Ultrastrong photon–magnon coupling has been reported for an yttrium–iron–garnet sphere embedded in a cavity with a resonance frequency in the gigahertz region[60–64], where the electromagnetic wave was confined by metallic or superconducting mirrors. Recently, $g/\omega \sim 0.46$ has been achieved to detect dark matter (galactic axions)[65]. Ultrastrong spin–magnon[31] and magnon–magnon[66,67] couplings have also been observed. However, evidence of an SRPT has not been reported even with those magnonic ultrastrong couplings, although various phase transitions exist in magnetic systems, and it is conceivable that some of the known phase transitions can be understood as the SRPT or an analogue.

The LTPT in ErFeO$_3$ has been discussed in relation to the cooperative Jahn–Teller transition[29,41,42], which is analogous to the SRPT[68,69]. Vitebskii and Yablonskii proposed a theoretical model for describing the LTPT in 1978[30]. Further, Kadomtseva et al. theoretically investigated the ratio between the Er^{3+}–Er^{3+} and Er^{3+}–Fe^{3+} interaction strengths in 1980[29]. They also mentioned the analogy between the LTPT and cooperative Jahn–Teller transition[41,42]. Loos and Larson discussed the analogy between the cooperative Jahn–Teller transition and SRPT in 1984 and 2008, respectively[68,69]. However, the analogy between the LTPT and SRPT has not been directly drawn either theoretically or experimentally because the analogies between the LTPT and cooperative Jahn–Teller transition and between the latter and the SRPT have been independently discussed[29,68,69], and no experimental evidence has been shown. The spin-Peierls transitions[70,71] and the spin-reorientation transition in rare-earth iron garnets[72] have also been discussed as analogous phenomena to the SRPT. However, no experimental evidence has been demonstrated. Structural transitions in ferroelectric materials may also be seen as a SRPT analogue at a first glance[73]. However, when we map such ferroelectric systems to the Dicke model, we find that the resonance frequency of the electric polarization becomes an imaginary value, which indicates that such ferroelectric phase transitions are caused by the instability of the electric polarization subsystem rather than by the coupling between the polarization and phonon subsystems. Hence, no other SRPT analogue by matter–matter coupling has been confirmed quantitatively.

In 2018, the $\sqrt{N}$-dependence (N is the Er^{3+} density) of the anticrossing frequency, or vacuum Rabi splitting ($2g$), between paramagnetic Er^{3+} spins and a Fe^{3+} magnon mode was experimentally confirmed at $T > T_c$[31]. This $\sqrt{N}$-dependence, the Dicke

cooperativity, can be taken as evidence that the coupling between the Er^{3+} spin ensemble and Fe^{3+} magnon mode is cooperative, being well described by the Dicke model or its extension.

This study provides the quantitative evidence of magnonic SRPT manifestation. Meanwhile, the existence of photonic SRPT, which was originally proposed in 1973, has yet to be confirmed. Moreover, the possibility of its theoretical existence in materials with spin degree of freedom is still under debate[36,37,58,59]. Since the development of the Dicke model, this study is the first to elucidate the occurrence of magnonic thermal-equilibrium SRPT in an actual material, namely ErFeO$_3$.

Conclusions

In this study, using an ErFeO$_3$ spin model reproducing both the phase diagrams obtained via magnetization measurements[26] and terahertz magnetospectroscopy results[31], we derived an extended Dicke Hamiltonian that accounts for Er^{3+}–Er^{3+} exchange interactions as well as the cooperative coupling between the Er^{3+} spins and Fe^{3+} magnon modes. We found that the LTPT in ErFeO$_3$ can be caused solely by Er^{3+}–magnon coupling (in the absence of Er^{3+}–Er^{3+} exchange interactions). From the analytical correspondence between the spin and Dicke models and the quantitative verification that the Er^{3+}–magnon coupling solely causes the LTPT, we concluded that the LTPT in ErFeO$_3$ is a magnonic SRPT in the extended Dicke model. This is the first confirmation of the SRPT in thermal equilibrium since its proposal in 1973[1]. These results are expected to be the first step in finding the (originally proposed) photonic SRPT in magnetic or other materials explicitly including the spin degree of freedom.

The thermal SRPT in ErFeO$_3$ would exhibit rich physics beyond the quantum or zero-temperature SRPT that has been demonstrated in laser-driven cold atoms[14–17]. It is known that the thermal and quantum fluctuations of photons and atoms exhibit characteristic behaviours around the SRPT[74,75]. Recent studies have reported the occurrence of strong, two-mode quantum squeezing at the SRPT critical point[12,13]. In future endeavours, including ongoing terahertz magnetospectroscopy experiments on Er$_x$Y$_{1-x}$FeO$_3$[76] concerning LTPT and subsequent quantum-fluctuation measurements[77,78] of magnons and Er^{3+} spins, we intend to investigate the occurrence of such quantum-squeezing phenomena during thermal SRPT.

The generation of squeezed states of light has attracted considerable research interest over several decades because they facilitate precision measurements to be performed beyond the limitations encountered owing to the manifestation of quantum vacuum fluctuations and evolution of continuous-variable quantum computing. However, most existing squeezing-generation protocols require a system to be driven to realize transient squeezed states. This limits the realizable degree of squeezing during experiments owing to unpredictable noise. In contrast, quantum squeezing at the SRPT critical point can be stably realized under thermal equilibrium, because an ultrastrong coupled system remains at its most stable in the squeezed state. As a result, such systems are resilient to unpredictable noise. This fundamental stability and resilience are expected to facilitate the realization of novel applications exploring quantum sensing and decoherence-robust continuous-variable quantum computing via the occurrence of quantum squeezing at the SRPT critical point.

Methods

Parameters. Following our previous study[31], we used the following values for the Fe^{3+} subsystem in our numerical calculations, except A_x, which was determined to fit the spin resonance frequencies to the corresponding terahertz absorption spectrum in our experiments[31] (see "Spin resonance frequencies" in Supplementary Methods for details).

$$J_{Fe} = 4.96 \text{ meV}, \tag{26}$$

$$D_y^{\text{Fe}} = -0.107 \text{ meV}, \tag{27}$$

$$A_x = 0.0073 \text{ meV}, \tag{28}$$

$$A_z = 0.0150 \text{ meV}, \tag{29}$$

$$A_{xz} = 0. \tag{30}$$

The anisotropic g-factors for Er^{3+} spins were assumed to be

$$\mathfrak{g}_x^{\text{Er}} = 6, \tag{31}$$

$$\mathfrak{g}_y^{\text{Er}} = 3.4, \tag{32}$$

$$\mathfrak{g}_z^{\text{Er}} = 9.6. \tag{33}$$

These values were utilized to fit the Er^{3+} spin resonance frequencies depicted in Supplementary Figs. 1–3 to their corresponding absorption peak positions observed during experiments[31] (refer to "Spin resonance frequencies" in Supplementary Methods). They were multiplied by 2 compared to those estimated in our previous study[31] to compensate for the use of the additional factor of 1/2 in Eq. (8).

The anisotropic g-factors for Fe^{3+} spins were assumed to be

$$\mathfrak{g}_x^{\text{Fe}} = 2, \tag{34}$$

$$\mathfrak{g}_y^{\text{Fe}} = 2, \tag{35}$$

$$\mathfrak{g}_z^{\text{Fe}} = 0.6. \tag{36}$$

Here, $\mathfrak{g}_z^{\text{Fe}}$ was determined to reproduce the critical magnetic flux density $B_z^{\text{DC}} \sim 20 \text{ T}$[26] of the transition between the Γ_2 phase and the Γ_4 phase, in which the Fe^{3+} spins are ordered antiferromagnetically along the a axis with slight canting toward the c axis, in the case of $\mathbf{B}^{\text{DC}}//c$. On the other hand, $\mathfrak{g}_x^{\text{Fe}}$ and $\mathfrak{g}_y^{\text{Fe}}$ were simply set to the values in the case of free electron spin because the results in the present study are insensitive to these values.

Concerning the Er^{3+}–Er^{3+} and Er^{3+}–Fe^{3+} exchange interactions, we used the following values.

$$J_{\text{Er}} = 0.037 \text{ meV}, \tag{37}$$

$$J = 0.60 \text{ meV}, \tag{38}$$

$$D_x = 0.034 \text{ meV}, \tag{39}$$

$$D_y = 0.003 \text{ meV}. \tag{40}$$

These values were utilized to fit Fig. 2 roughly to the phase diagrams reported by Zhang et al.[26] The precise values of J_{Er}, J, and D_y were mainly determined to fit our calculated spin resonance frequencies $\mathbf{B}^{\text{DC}}//c$ to the corresponding terahertz absorption spectrum in our experiments[31], which are both shown in Supplementary Fig. 3a (see "Spin resonance frequencies" in Supplementary Methods). On the other hand, D_x was determined to reproduce $T_c = 4.0 \text{ K}$.

Although the ratio between the Er^{3+}–Er^{3+} and Er^{3+}–Fe^{3+} interaction strengths was theoretically investigated by the phase boundary for $\mathbf{B}^{\text{DC}}//a$[29], the phase diagrams (T_c and critical DC fields) themselves were not sufficient to determine all of our parameters, although we do not intend to claim the impossibility of such determination in the present study. The phase diagrams gave only some ranges of the parameters. Because the LTPT is caused by not only the Er^{3+}–Er^{3+} exchange interaction, but also the Er^{3+}–Fe^{3+} interactions (Er^{3+}–magnon couplings), there are at least four parameters (J_{Er}, J, D_x, and D_y) even if the number of parameters is reduced according to the analysis in "Reduction of number of parameters" in Supplementary Methods. The anisotropic g-factors $\mathfrak{g}_x^{\text{Er}}$, $\mathfrak{g}_y^{\text{Er}}$, and $\mathfrak{g}_z^{\text{Er}}$ of the Er^{3+} spins are free parameters, and could easily change the critical DC fields. T_c and three critical DC fields obtained from the magnetization measurements[26] were not sufficient to determine the above parameters.

In determining all of these quantities, the spin resonance frequencies were informative. In particular, as discussed in "Spin resonance frequencies" in Supplementary Methods using the extended Dicke Hamiltonian, the Er^{3+}–Er^{3+} exchange interaction strength J_{Er} clearly appears as the frequency splitting between the Er^{3+} in-phase and out-of-phase resonances. The out-of-phase mode cannot be excited by the terahertz wave unless it couples with the Fe^{3+} magnon modes. In that sense, the anti-crossing between the Er^{3+} in-phase resonances, out-of-phase resonances, and Fe^{3+} qFM magnon mode $B_z^{\text{DC}} \sim 4 \text{ T}$ in Supplementary Fig. 3 provides the most important information for determining J_{Er} and the other parameters (see "Spin resonance frequencies" in Supplementary Methods).

Mean-field calculation method. Because we simply considered a homogeneous $\mathbf{B}^{\text{DC}}$ in this study, the expectation values of the Er^{3+} spins $\boldsymbol{\sigma}^{\text{A/B}} \equiv \langle \hat{\boldsymbol{\sigma}}_i^{\text{A/B}} \rangle$ and Fe^{3+} spins $\mathbf{S}^{\text{A/B}} \equiv \langle \hat{\mathbf{S}}_i^{\text{A/B}} \rangle$ were independent of the site index i. The brackets represent the theoretical expectation values of the operators at a finite temperature in the Heisenberg representation. The brackets also correspond to the ensemble average of the spins in each sublattice. Their equations of motion can be obtained from the Heisenberg equations derived from the Hamiltonian in Eq. (2), as follows ($s = $ A, B).

$$\hbar(\partial/\partial t)\boldsymbol{\sigma}^s = -\boldsymbol{\sigma}^s \times \mathfrak{g}\mu_B \mathbf{B}_{\text{Er}}^s(\{\boldsymbol{\sigma}^{\text{A/B}}\}, \{\mathbf{S}^{\text{A/B}}\}), \tag{41}$$

$$\hbar(\partial/\partial t)\mathbf{S}^s = -\mathbf{S}^s \times \mathfrak{g}\mu_B \mathbf{B}_{\text{Fe}}^s(\{\boldsymbol{\sigma}^{\text{A/B}}\}, \{\mathbf{S}^{\text{A/B}}\}). \tag{42}$$

Here, $\mathbf{B}_{\text{Er}}^{\text{A/B}}$ and $\mathbf{B}_{\text{Fe}}^{\text{A/B}}$ are the mean fields for the Er^{3+} and Fe^{3+} spins, respectively, and they can be expressed as

$$\mathfrak{g}\mu_B \mathbf{B}_{\text{Er}}^{\text{A}}\left(\left\{\boldsymbol{\sigma}^{\text{A/B}}\right\}, \left\{\mathbf{S}^{\text{A/B}}\right\}\right) = \mu_B \mathfrak{g}^{\text{Er}} \cdot \mathbf{B}^{\text{DC}} + 2z_{\text{Er}}J_{\text{Er}}\boldsymbol{\sigma}^{\text{B}}$$
$$+ \sum_{s=\text{A,B}} 2 \begin{pmatrix} JS_x^s - (\mathbf{D}^{\text{A},s} \times \mathbf{S}^s)_x \\ 0 \\ JS_z^s - (\mathbf{D}^{\text{A},s} \times \mathbf{S}^s)_z \end{pmatrix}, \tag{43}$$

$$\mathfrak{g}\mu_B \mathbf{B}_{\text{Er}}^{\text{B}}\left(\left\{\boldsymbol{\sigma}^{\text{A/B}}\right\}, \left\{\mathbf{S}^{\text{A/B}}\right\}\right) = \mu_B \mathfrak{g}^{\text{Er}} \cdot \mathbf{B}^{\text{DC}} + 2z_{\text{Er}}J_{\text{Er}}\boldsymbol{\sigma}^{\text{A}}$$
$$+ \sum_{s=\text{A,B}} 2 \begin{pmatrix} JS_x^s - (\mathbf{D}^{\text{B},s} \times \mathbf{S}^s)_x \\ 0 \\ JS_z^s - (\mathbf{D}^{\text{B},s} \times \mathbf{S}^s)_z \end{pmatrix}, \tag{44}$$

$$\mathfrak{g}\mu_B \mathbf{B}_{\text{Fe}}^{\text{A}}(\{\boldsymbol{\sigma}^{\text{A/B}}\}, \{\mathbf{S}^{\text{A/B}}\}) = \mu_B \mathfrak{g}^{\text{Fe}} \cdot \mathbf{B}^{\text{DC}} + \sum_{s=\text{A,B}} x(J\boldsymbol{\sigma}^s + \mathbf{D}^{s,\text{A}} \times \boldsymbol{\sigma}^s)$$
$$+ \begin{pmatrix} z_{\text{Fe}}J_{\text{Fe}}S_x^{\text{B}} + z_{\text{Fe}}D_y^{\text{Fe}}S_z^{\text{B}} - 2A_xS_x^{\text{A}} - A_{xz}S_z^{\text{A}} \\ z_{\text{Fe}}J_{\text{Fe}}S_y^{\text{B}} \\ z_{\text{Fe}}J_{\text{Fe}}S_z^{\text{B}} - z_{\text{Fe}}D_y^{\text{Fe}}S_x^{\text{B}} - 2A_zS_z^{\text{A}} - A_{xz}S_x^{\text{A}} \end{pmatrix}, \tag{45}$$

$$\mathfrak{g}\mu_B \mathbf{B}_{\text{Fe}}^{\text{B}}(\{\boldsymbol{\sigma}^{\text{A/B}}\}, \{\mathbf{S}^{\text{A/B}}\}) = \mu_B \mathfrak{g}^{\text{Fe}} \cdot \mathbf{B}^{\text{DC}} + \sum_{s=\text{A,B}} x(J\boldsymbol{\sigma}^s + \mathbf{D}^{s,\text{B}} \times \boldsymbol{\sigma}^s)$$
$$+ \begin{pmatrix} z_{\text{Fe}}J_{\text{Fe}}S_x^{\text{A}} - z_{\text{Fe}}D_y^{\text{Fe}}S_z^{\text{A}} - 2A_xS_x^{\text{B}} + A_{xz}S_z^{\text{B}} \\ z_{\text{Fe}}J_{\text{Fe}}S_y^{\text{A}} \\ z_{\text{Fe}}J_{\text{Fe}}S_z^{\text{A}} + z_{\text{Fe}}D_y^{\text{Fe}}S_x^{\text{A}} - 2A_zS_z^{\text{B}} + A_{xz}S_x^{\text{B}} \end{pmatrix}. \tag{46}$$

In Eqs. (43) and (44), the first, second, and third terms represent the Zeeman effect, Er^{3+}–Er^{3+} exchange interaction, and Er^{3+}–Fe^{3+} exchange interaction, respectively. In Eqs. (45) and (46), the first, second, and third terms represent the Zeeman effect, Er^{3+}–Fe^{3+} exchange interaction, and Fe^{3+}–Fe^{3+} exchange interaction, respectively. The dilution of the Er^{3+} spins is reflected by the factors $z_{\text{Er}} = 6x$ and x. z_{Er} denotes the number of neighbours of Er^{3+}, and its value effectively decreases by a factor of x. Because $(1/2)\hat{\boldsymbol{\sigma}}^{\text{A/B}}$ corresponds to the spin $\frac{1}{2}$ operator, a factor of 2 appears overall in Eqs. (43) and (44). As explained at the end of the section "$ErFeO_3$," the y component of the third term in Eqs. (43) and (44) is set to zero by means of implicitly considering a high-energy potential.

The free energy of the system is minimized when the thermal equilibrium values (time averages) of spins $\bar{\boldsymbol{\sigma}}^{\text{A/B}}$ and $\bar{\mathbf{S}}^{\text{A/B}}$ are parallel to their mean fields $\bar{\mathbf{B}}_{\text{Er}}^s \equiv \mathbf{B}_{\text{Er}}^s(\{\bar{\boldsymbol{\sigma}}^{\text{A/B}}\}, \{\bar{\mathbf{S}}^{\text{A/B}}\})$ and $\bar{\mathbf{B}}_{\text{Fe}}^s \equiv \mathbf{B}_{\text{Fe}}^s(\{\bar{\boldsymbol{\sigma}}^{\text{A/B}}\}, \{\bar{\mathbf{S}}^{\text{A/B}}\})$ as follows.

$$\bar{\boldsymbol{\sigma}}^s = \langle \hat{\boldsymbol{\sigma}}^s \rangle = \langle \hat{\sigma}_{\parallel}^s \rangle \mathbf{u}_{\text{Er}}^s, \quad \hat{\sigma}_{\parallel}^s \equiv \hat{\boldsymbol{\sigma}}^s \cdot \mathbf{u}_{\text{Er}}^s, \tag{47}$$

$$\bar{\mathbf{S}}^s = \langle \hat{\mathbf{S}}^s \rangle = \langle \hat{S}_{\parallel}^s \rangle \mathbf{u}_{\text{Fe}}^s, \quad \hat{S}_{\parallel}^s \equiv \hat{\mathbf{S}}^s \cdot \mathbf{u}_{\text{Fe}}^s. \tag{48}$$

Here, the unit vectors of the mean fields are defined as

$$\mathbf{u}_{\text{Er}}^s \equiv \bar{\mathbf{B}}_{\text{Er}}^s / |\bar{\mathbf{B}}_{\text{Er}}^s|, \tag{49}$$

$$\mathbf{u}_{\text{Fe}}^s \equiv \bar{\mathbf{B}}_{\text{Fe}}^s / |\bar{\mathbf{B}}_{\text{Fe}}^s|. \tag{50}$$

The thermal equilibrium values $\bar{\boldsymbol{\sigma}}^{\text{A/B}}$ and $\bar{\mathbf{S}}^{\text{A/B}}$ can be determined as follows. For given mean fields $\bar{\mathbf{B}}_{\text{Fe}}^s$ and $\bar{\mathbf{B}}_{\text{Er}}^s$, the effective Hamiltonians of each Er^{3+} and Fe^{3+} can be defined as

$$\hat{\mathcal{H}}_{\text{Er}}^s = \frac{1}{2}\mathfrak{g}\mu_B \hat{\boldsymbol{\sigma}}^s \cdot \bar{\mathbf{B}}_{\text{Er}}^s = \frac{1}{2}\mathfrak{g}\mu_B \hat{\sigma}_{\parallel}^s |\bar{\mathbf{B}}_{\text{Er}}^s|, \tag{51}$$

$$\hat{\mathcal{H}}_{\text{Fe}}^s = \mathfrak{g}\mu_B \hat{\mathbf{S}}^s \cdot \bar{\mathbf{B}}_{\text{Fe}}^s = \mathfrak{g}\mu_B \hat{S}_{\parallel}^s |\bar{\mathbf{B}}_{\text{Fe}}^s|. \tag{52}$$

Subsequently, the partition functions can be expressed as

$$Z_{\mathrm{Er}}^s \equiv \mathrm{Tr}\left[\mathrm{e}^{-\hat{\mathcal{H}}_{\mathrm{Er}}^s/(k_B T)}\right] = \sum_{m=\pm 1} \mathrm{e}^{-my_s} = 2\cosh(y_s), \quad (53)$$

$$Z_{\mathrm{Fe}}^s \equiv \mathrm{Tr}\left[\mathrm{e}^{-\hat{\mathcal{H}}_{\mathrm{Fe}}^s/(k_B T)}\right] = \sum_{m=-S}^{S} \mathrm{e}^{-mx_s} = \frac{\sinh[(S+1/2)x_s]}{\sinh(x_s/2)}, \quad (54)$$

where the following are defined.

$$y_s \equiv \mathfrak{g}\mu_B |\bar{\mathbf{B}}_{\mathrm{Er}}^s|/(2k_B T), \quad (55)$$

$$x_s \equiv \mathfrak{g}\mu_B |\bar{\mathbf{B}}_{\mathrm{Fe}}^s|/(k_B T). \quad (56)$$

Because $\hat{\boldsymbol{\sigma}}^{A/B}$ is not a standard spin operator with an angular momentum of $\hbar$ or $\hbar/2$ but is a vector of the Pauli operators, the summation is performed for $m = \pm 1$. The free energies are given as $-k_B T \ln Z_{\mathrm{Er}}^{A/B}$ and $-k_B T \ln Z_{\mathrm{Fe}}^{A/B}$, and the thermal equilibrium values of the spins are

$$\langle \hat{\sigma}_\parallel^s \rangle = -\frac{\partial}{\partial y_s} \ln Z_{\mathrm{Er}}^s = -\tanh(y_s), \quad (57)$$

$$\langle \hat{S}_\parallel^s \rangle = -\frac{\partial}{\partial x_s} \ln Z_{\mathrm{Fe}}^s = -SB_S(Sx_s), \quad (58)$$

where $B_S(z)$ is the Brillouin function, defined as

$$B_J(z) \equiv \frac{2J+1}{2J}\coth\left(\frac{2J+1}{2J}z\right) - \frac{1}{2J}\coth\left(\frac{z}{2J}\right). \quad (59)$$

By consistently solving Eqs. (43)–(48), (57) and (58), $\bar{\boldsymbol{\sigma}}^{A/B}$ and $\bar{\mathbf{S}}^{A/B}$ can be determined at finite temperatures.

Derivation of extended Dicke Hamiltonian. Here, we describe the transformation of our spin model, Eq. (2), into an extended version of the Dicke Hamiltonian, Eq. (1). We first rewrite the Fe^{3+} subsystem $\mathcal{H}_{\mathrm{Fe}}$ in terms of the annihilation and creation operators of a magnon in "Fe^{3+} subsystem." The Er^{3+} subsystem $\mathcal{H}_{\mathrm{Er}}$ is rewritten using large spin operators in "Er^{3+} subsystems." The Er^{3+}–Fe^{3+} exchange interactions, $\mathcal{H}_{\mathrm{Er-Fe}}$, are transformed into five Er^{3+}–magnon couplings as per "Er^{3+}−Fe^{3+} interactions." Finally, the extended Dicke Hamiltonian is discussed in the section "Total Hamiltonian."

Fe^{3+} subsystem. We assume that the most stable values of the Fe^{3+} spins at zero temperature, $\bar{\mathbf{S}}^{A/B}$, are unchanged even when $\mathbf{B}^{DC}$ ($\lesssim 10\,\mathrm{T}$) is applied, as we also assumed in our previous studies[31,34]. Under this assumption, as depicted in Fig. 1a, the most stable state (i.e., the ground state) of the Fe^{3+} subsystem $\hat{\mathcal{H}}_{\mathrm{Fe}}$, Eq. (3), can be expressed as

$$\bar{\mathbf{S}}_0^A = \begin{pmatrix} S\sin\beta_0 \\ 0 \\ -S\cos\beta_0 \end{pmatrix}, \bar{\mathbf{S}}_0^B = \begin{pmatrix} S\sin\beta_0 \\ 0 \\ S\cos\beta_0 \end{pmatrix}. \quad (60)$$

Here, the canting angle β_0 can be expressed as (see "Magnon quantization" in Supplementary Methods and Supplementary Fig. 4 or refs. [31,33,34])

$$\beta_0 = -\frac{1}{2}\arctan\frac{A_{xy} + z_{\mathrm{Fe}} D_y^{\mathrm{Fe}}}{z_{\mathrm{Fe}} J_{\mathrm{Fe}} - A_x + A_z}. \quad (61)$$

The magnon is the quantum of spin fluctuations (spin waves) from this stable state. As shown in "Magnon quantization" in Supplementary Methods as well as in refs. [31,34] in the long-wavelength limit, the Fe^{3+} Hamiltonian $\hat{\mathcal{H}}_{\mathrm{Fe}}$, Eq. (3), can be rewritten in terms of the annihilation (creation) operators $\hat{a}_K$ ($\hat{a}_K^\dagger$) of Fe^{3+} magnons as

$$\hat{\mathcal{H}}_{\mathrm{Fe}} \approx \sum_{K=0,\pi} \hbar\omega_K \hat{a}_K^\dagger \hat{a}_K + \text{const.} \quad (62)$$

Here, $K = 0$ and π correspond to the qFM and qAFM magnon modes, respectively[33]. The eigenfrequencies can be expressed as follows.

$$\omega_K = \gamma\sqrt{(b\cos K - a)(d\cos K + c)}. \quad (63)$$

Here, we define

$$a = [S/(\mathfrak{g}\mu_B)]\big[-A_z - A_x - (z_{\mathrm{Fe}}J_{\mathrm{Fe}} + A_z - A_x)\cos(2\beta_0)$$
$$+ (A_{xz} + z_{\mathrm{Fe}}D_y^{\mathrm{Fe}})\sin(2\beta_0)\big], \quad (64)$$

$$b = [S/(\mathfrak{g}\mu_B)](z_{\mathrm{Fe}}J_{\mathrm{Fe}}), \quad (65)$$

$$c = [S/(\mathfrak{g}\mu_B)][(z_{\mathrm{Fe}}J_{\mathrm{Fe}} + 2A_z - 2A_x)\cos(2\beta_0) + z_{\mathrm{Fe}}D_y^{\mathrm{Fe}}\sin(2\beta_0)], \quad (66)$$

$$d = [S/(\mathfrak{g}\mu_B)][-z_{\mathrm{Fe}}J_{\mathrm{Fe}}\cos(2\beta_0) - (2A_{xz} + z_{\mathrm{Fe}}D_y^{\mathrm{Fe}})\sin(2\beta_0)]. \quad (67)$$

The operators of the spin fluctuations $\delta\hat{\mathbf{S}}_i^{A/B} \equiv \hat{\mathbf{S}}_i^{A/B} - \bar{\mathbf{S}}_0^{A/B}$ can be expressed as

$$\delta\hat{\mathbf{S}}_i^A = \sqrt{\frac{S}{2N_0}}\begin{pmatrix} -(\hat{T}_0 - \hat{T}_\pi)\cos\beta_0 \\ (\hat{Y}_0 - \hat{Y}_\pi) \\ -(\hat{T}_0 - \hat{T}_\pi)\sin\beta_0 \end{pmatrix}, \quad (68)$$

$$\delta\hat{\mathbf{S}}_i^B = \sqrt{\frac{S}{2N_0}}\begin{pmatrix} (\hat{T}_0 + \hat{T}_\pi)\cos\beta_0 \\ (\hat{Y}_0 + \hat{Y}_\pi) \\ -(\hat{T}_0 + \hat{T}_\pi)\sin\beta_0 \end{pmatrix}, \quad (69)$$

where the following are defined.

$$\hat{T}_K \equiv \left(\frac{b\cos K - a}{d\cos K + c}\right)^{1/4}\frac{(\hat{a}_{-K}^\dagger + \hat{a}_K)}{\sqrt{2}}, \quad (70)$$

$$\hat{Y}_K \equiv \left(\frac{d\cos K + c}{b\cos K - a}\right)^{1/4}\frac{\mathrm{i}(\hat{a}_{-K}^\dagger - \hat{a}_K)}{\sqrt{2}}. \quad (71)$$

For the subsequent discussion, we define the sum and difference of the spins as

$$\hat{\mathbf{S}}_i^\pm \equiv \hat{\mathbf{S}}_i^A \pm \hat{\mathbf{S}}_i^B. \quad (72)$$

Their equilibrium (most stable) values are

$$\bar{\mathbf{S}}_0^+ \equiv \bar{\mathbf{S}}_0^A + \bar{\mathbf{S}}_0^B = (2S\sin\beta_0, 0, 0)^t, \quad (73)$$

$$\bar{\mathbf{S}}_0^- \equiv \bar{\mathbf{S}}_0^A - \bar{\mathbf{S}}_0^B = (0, 0, -2S\cos\beta_0)^t, \quad (74)$$

and their fluctuations are given by the sum and difference of Eqs. (68) and (69) as follows.

$$\delta\hat{\mathbf{S}}^+ \equiv \delta\hat{\mathbf{S}}_i^A + \delta\hat{\mathbf{S}}_i^B = \sqrt{\frac{2S}{N_0}}\begin{pmatrix} \hat{T}_\pi\cos\beta_0 \\ \hat{Y}_0 \\ -\hat{T}_0\sin\beta_0 \end{pmatrix}, \quad (75)$$

$$\delta\hat{\mathbf{S}}^- \equiv \delta\hat{\mathbf{S}}_i^A - \delta\hat{\mathbf{S}}_i^B = \sqrt{\frac{2S}{N_0}}\begin{pmatrix} -\hat{T}_0\cos\beta_0 \\ -\hat{Y}_\pi \\ \hat{T}_\pi\sin\beta_0 \end{pmatrix}. \quad (76)$$

Er^{3+} subsystems. We define the following new operators.

$$\hat{\boldsymbol{\Sigma}}^{A/B} \equiv \frac{1}{2}\sum_{i=1}^{N_0}\hat{\mathbf{R}}_i^{A/B}. \quad (77)$$

For an Er^{3+} ion, $(1/2)\hat{\mathbf{R}}_i^{A/B}$ is a spin $\frac{1}{2}$ operator and $\hat{\boldsymbol{\Sigma}}^{A/B}$ is a spin $\frac{N}{4}$ operator representing the rare earth spins in the A/B sublattice. We also define the sum and difference of the two sublattice spins as

$$\hat{\boldsymbol{\Sigma}}^\pm \equiv \hat{\boldsymbol{\Sigma}}^A \pm \hat{\boldsymbol{\Sigma}}^B. \quad (78)$$

In the long-wavelength limit, all spins in each sublattice have the same values in both static and dynamic situations. Subsequently, the Er^{3+} Hamiltonian in Eq. (6) can be rewritten as

$$\hat{\mathcal{H}}_{\mathrm{Er}} \approx \sum_{\xi=x,y,z}\mathfrak{g}_\xi^{\mathrm{Er}}\mu_B\hat{\Sigma}_\xi^+ B_\xi^{DC} + z_{\mathrm{Er}}J_{\mathrm{Er}}\sum_{i=1}^{N_0}\hat{\mathbf{R}}_i^A \cdot \sum_{i'=1}^{N_0}\frac{\hat{\mathbf{R}}_{i'}^B}{xN_0} \quad (79)$$

$$= \sum_{\xi=x,y,z}\mathfrak{g}_\xi^{\mathrm{Er}}\mu_B\hat{\Sigma}_\xi^+ B_\xi^{DC} + \frac{8z_{\mathrm{Er}}J_{\mathrm{Er}}}{N}\hat{\boldsymbol{\Sigma}}^A \cdot \hat{\boldsymbol{\Sigma}}^B. \quad (80)$$

Er^{3+}–Fe^{3+} interactions. In the same manner as in our prior works[31,34], the Hamiltonian of the Er^{3+}–Fe^{3+} exchange interactions can be rewritten using Eq. (11), as

$$\hat{\mathcal{H}}_{\mathrm{Er-Fe}} \approx 2J\left(\hat{\boldsymbol{\Sigma}}^+ \cdot \bar{\mathbf{S}}_0^+ + \hat{\boldsymbol{\Sigma}}^+ \cdot \delta\hat{\mathbf{S}}^+\right) + \begin{pmatrix} 0 \\ 2D_y \\ 0 \end{pmatrix} \cdot \left(\hat{\boldsymbol{\Sigma}}^+ \times \bar{\mathbf{S}}_0^- + \hat{\boldsymbol{\Sigma}}^+ \times \delta\hat{\mathbf{S}}^-\right)$$

$$+ \begin{pmatrix} 2D_x \\ 0 \\ 0 \end{pmatrix} \cdot \left(\hat{\boldsymbol{\Sigma}}^- \times \bar{\mathbf{S}}_0^- + \hat{\boldsymbol{\Sigma}}^- \times \delta\hat{\mathbf{S}}^-\right). \quad (81)$$

In each set of parentheses, the first term represents the influence of the static components (equilibrium values) $\bar{\mathbf{S}}_0^{A/B}$ of Fe^{3+} spins to Er^{3+} spins $\hat{\boldsymbol{\Sigma}}^\pm$, and the second term represents the coupling between the Fe^{3+} fluctuation $\delta\hat{\mathbf{S}}^\pm$ and Er^{3+} spins $\hat{\boldsymbol{\Sigma}}^\pm$. We divide these terms into two Hamiltonians as

$$\hat{\mathcal{H}}_{\mathrm{Er-Fe}} \approx \hat{\mathcal{H}}_{\mathrm{Er-Fe}}^\Sigma + \hat{\mathcal{H}}_{\mathrm{Er-Fe}}^{\mathrm{coupling}}. \quad (82)$$

The first term gives part of the Er^{3+} spin resonance frequency and can be expressed as follows.

$$\hat{\mathcal{H}}^{\Sigma}_{Er-Fe} = E_x \hat{\Sigma}^+_x. \tag{83}$$

Here, we used Eqs. (73), (74) and (18). We neglected $(-4SD_x \cos\beta_0)\hat{\Sigma}^-_y$ under the assumption explained at the end of the section "$ErFeO_3$." The second term in Eq. (82) can be rewritten in terms of the Fe^{3+} fluctuations as

$$\hat{\mathcal{H}}^{coupling}_{Er-Fe} = \sqrt{\frac{8S}{N_0}}\Big[(J\cos\beta_0 - D_y \sin\beta_0)\hat{T}_\pi\hat{\Sigma}^+_x + J\hat{Y}_0\hat{\Sigma}^+_y + (D_x \sin\beta_0)\hat{T}_\pi\hat{\Sigma}^-_y$$
$$+ D_x\hat{Y}_\pi\hat{\Sigma}^-_z + (-J\sin\beta_0 - D_y\cos\beta_0)\hat{T}_0\hat{\Sigma}^+_z\Big]. \tag{84}$$

Total Hamiltonian. In terms of the annihilation and creation operators of magnons, the total Hamiltonian can be expressed as

$$\hat{\mathcal{H}} \approx \sum_{K=0,\pi} \hbar\omega_K \hat{a}^\dagger_K \hat{a}_K + E_x\hat{\Sigma}^+_x + \sum_{\xi=x,y,z} g^{Er}_\xi \mu_B B^{DC}_\xi \hat{\Sigma}^+_\xi + \frac{8z_{Er}J_{Er}}{N}\hat{\Sigma}^A \cdot \hat{\Sigma}^B$$

$$+ \frac{2\hbar g_x}{\sqrt{N}}(\hat{a}^\dagger_\pi + \hat{a}_\pi)\hat{\Sigma}^+_x + \frac{i2\hbar g_y}{\sqrt{N}}(\hat{a}^\dagger_0 - \hat{a}_0)\hat{\Sigma}^+_y + \frac{2\hbar g_{y'}}{\sqrt{N}}(\hat{a}^\dagger_\pi + \hat{a}_\pi)\hat{\Sigma}^-_y$$

$$+ \frac{i2\hbar g_z}{\sqrt{N}}(\hat{a}^\dagger_\pi - \hat{a}_\pi)\hat{\Sigma}^-_z + \frac{2\hbar g_{z'}}{\sqrt{N}}(\hat{a}^\dagger_0 + \hat{a}_0)\hat{\Sigma}^+_z. \tag{85}$$

The five coupling strengths are defined as

$$\hbar g_x = \sqrt{2xS}(J\cos\beta_0 - D_y\sin\beta_0)\left(\frac{b+a}{d-c}\right)^{1/4} = h \times \sqrt{x} \times 0.051\,\text{THz}, \tag{86}$$

$$\hbar g_y = \sqrt{2xS}J\left(\frac{d+c}{b-a}\right)^{1/4} = h \times \sqrt{x} \times 0.041\,\text{THz}, \tag{87}$$

$$\hbar g_{y'} = \sqrt{2xS}(D_x\sin\beta_0)\left(\frac{b+a}{d-c}\right)^{1/4} = h \times \sqrt{x} \times 3.1 \times 10^{-5}\,\text{THz}, \tag{88}$$

$$\hbar g_z = \sqrt{2xS}D_x\left(\frac{d-c}{b+a}\right)^{1/4} = h \times \sqrt{x} \times 0.116\,\text{THz}, \tag{89}$$

$$\hbar g_{z'} = \sqrt{2xS}(-J\sin\beta_0 - D_y\cos\beta_0)\left(\frac{b-a}{d+c}\right)^{1/4} = h \times \sqrt{x} \times (-0.040\,\text{THz}). \tag{90}$$

The actual values were evaluated using the parameters shown in "Parameters."

Compared with the expressions in our previous studies[31,34], the coupling strengths in Eqs. (86)–(87) include additional factors $\sqrt{2}$ and $\sqrt{S}$. First, $\sqrt{2}$ originates from the number of Er^{3+} sublattices in the present study, whereas a single Er^{3+} lattice was considered in our previous studies[31,34]. The second factor, $\sqrt{S}$, is a result of the difference in the method of normalizing the Fe^{3+} spins between the present and previous studies[31,34].

Whereas the Er^{3+} spin ensemble is described by six operators $\hat{\Sigma}^+_{x,y,z}$ and $\hat{\Sigma}^-_{x,y,z}$ in the extended Dicke Hamiltonian in Eq. (85), only $\hat{\Sigma}^+_x$ and $\hat{\Sigma}^-_z$ are relevant to the LTPT shown in Fig. 1. $\hat{\Sigma}^+_x$ corresponds to the paramagnetic alignment by the Fe^{3+} magnetization along the a axis, and $\hat{\Sigma}^-_z$ corresponds to the antiferromagnetic ordering along the c axis. Subsequently, to analyse the thermal equilibrium values of the spins, it is sufficient to consider only the following two terms in the Er^{3+}–Er^{3+} exchange interactions.

$$\frac{8z_{Er}J_{Er}}{N}\hat{\Sigma}^A \cdot \hat{\Sigma}^B = \frac{2z_{Er}J_{Er}}{N}\sum_{\xi=x,y,z}\left[(\hat{\Sigma}^+_\xi)^2 - (\hat{\Sigma}^-_\xi)^2\right]$$

$$\rightarrow \frac{2z_{Er}J_{Er}}{N}\left[(\hat{\Sigma}^+_x)^2 - (\hat{\Sigma}^-_z)^2\right]. \tag{91}$$

In contrast, while the Fe^{3+} spins are described by the qFM and qAFM magnon modes in Eq. (85), only the qAFM mode is relevant to the LTPT. As shown in Fig. 1, $\delta\hat{S}^-_y$ and $\delta\hat{S}^-_z$ are required to describe the rotation of the Fe^{3+} AFM vector in the bc plane, and $\delta\hat{S}^+_x$ is required for possible modulation of canting along the a axis. As seen in Eqs. (75) and (76), $\delta\hat{S}^+_x$, $\delta\hat{S}^-_y$, and $\delta\hat{S}^-_z$ are related to the qAFM magnon mode ($K = \pi$), and the qFM mode ($K = 0$) plays no role in the LTPT.

Consequently, among the terms in the total Hamiltonian given by Eq. (85), it is only necessary to consider the terms shown in Eq. (16) to describe the LTPT (the other terms are required to fully reproduce the terahertz spectra discussed in "Spin resonance frequencies" in Supplementary Methods). Note that, in Eq. (16), we

rewrote the large spin operators representing the Er^{3+} spin ensemble as

$$\begin{cases} \hat{\Sigma}^+_x \rightarrow \hat{\Sigma}_x \equiv \sum_{i=1}^N \hat{\sigma}_{i,x}/2 \\ \hat{\Sigma}^-_y \rightarrow \hat{\Sigma}_y \equiv \sum_{i=1}^N \hat{\sigma}_{i,y}/2\,, \\ \hat{\Sigma}^-_z \rightarrow \hat{\Sigma}_z \equiv \sum_{i=1}^N \hat{\sigma}_{i,z}/2 \end{cases} \tag{92}$$

where we re-indexed the Pauli operators representing the Er^{3+} spins in the two sublattices as

$$\begin{cases} \hat{\sigma}^A_{i,x} \rightarrow \hat{\sigma}_{2i-1,x} \\ \hat{\sigma}^A_{i,y} \rightarrow \hat{\sigma}_{2i-1,y}\,, \\ \hat{\sigma}^A_{i,z} \rightarrow \hat{\sigma}_{2i-1,z} \end{cases} \begin{cases} \hat{\sigma}^B_{i,x} \rightarrow \hat{\sigma}_{2i,x} \\ \hat{\sigma}^B_{i,y} \rightarrow -\hat{\sigma}_{2i,y}\,. \\ \hat{\sigma}^B_{i,z} \rightarrow -\hat{\sigma}_{2i,z} \end{cases} \tag{93}$$

Further, in Eq. (16), it was assumed that the external DC magnetic field is applied along the a axis to maintain Γ_{12} symmetry, where either $|\bar{\sigma}^A_z - \bar{\sigma}^B_z|$ or the rotation angle φ of the Fe^{3+} AFM vector from the c axis can be the order parameter for the LTPT. Among the five Er^{3+}–magnon couplings in Eq. (85), only the g_x and g_z terms are required to consider the coupling between $\hat{\Sigma}_{x,z}$ and the qAFM magnons. Although the $g_{y'}$ term also couples $\hat{\Sigma}_y$ and qAFM magnons, its coupling strength is negligible compared with $g_{x,z}$, as shown in Eq. (88), which is consistent with the experimentally observed antiferromagnetic ordering of the Er^{3+} spins along the c axis ($\langle\hat{\Sigma}_y\rangle = 0$).

As demonstrated in Figs. 4 and 5, the LTPT can be quantitatively reproduced as the SRPT in the extended Dicke Hamiltonian, Eq. (85), which was derived from the spin model of $ErFeO_3$. The essential terms were extracted as shown in Eq. (16). The g_z term (antisymmetric Er^{3+}–Fe^{3+} exchange interaction with D_x) corresponds to the matter–photon coupling and causes the antiferromagnetic ordering of Er^{3+} spins along the c axis and the b component of the Fe^{3+} spins through the spontaneous appearance of qAFM magnons.

Semiclassical calculation method. Wang and Hioe demonstrated a simple calculation method for the SRPT in 1973[2], and Hepp and Lieb confirmed its validity for the Dicke model[47]. In the Dicke model, the partition function at temperature T

$$\mathcal{Z}_{Dicke}(T) \equiv \text{Tr}[e^{-\hat{\mathcal{H}}_{Dicke}/(k_B T)}], \tag{94}$$

in the thermodynamic limit $N \rightarrow \infty$ can be approximately evaluated by replacing the trace over the photonic variables with an integral over coherent states $|\sqrt{N}\bar{a}\rangle$ ($\bar{a} \in \mathbb{C}$; giving $\hat{a}|\sqrt{N}\bar{a}\rangle = \sqrt{N}\bar{a}|\sqrt{N}\bar{a}\rangle$) as

$$\bar{\mathcal{Z}}_{Dicke}(T) \equiv \int \frac{d^2\bar{a}}{\pi/N}\text{Tr}[e^{-\hat{\mathcal{H}}^{eff}_{Dicke}(\bar{a})/(k_B T)}] \tag{95}$$

$$= \int \frac{d^2\bar{a}}{\pi/N}e^{-\bar{\mathcal{S}}_{Dicke}(\bar{a},T)/(k_B T)}, \tag{96}$$

where an effective Hamiltonian is defined as given below,

$$\frac{\hat{\mathcal{H}}^{eff}_{Dicke}(\bar{a})}{\hbar} \equiv N\omega_{ph}|\bar{a}|^2 + \omega_{ex}\hat{S}_x + i2g(\bar{a}^* - \bar{a})\hat{S}_z, \tag{97}$$

as well as an action

$$\bar{\mathcal{S}}_{Dicke}(\bar{a}, T) \equiv -k_B T\ln\text{Tr}[e^{-\hat{\mathcal{H}}^{eff}_{Dicke}(\bar{a})/(k_B T)}] \tag{98}$$

$$= N\Big\{\hbar\omega_{ph}|\bar{a}|^2 - k_B T\ln\text{Tr}[e^{-\hat{\mathcal{H}}^a_{Dicke}(\bar{a})/(k_B T)}]\Big\}, \tag{99}$$

and an effective Hamiltonian per atom

$$\frac{\hat{\mathcal{H}}^a_{Dicke}(\bar{a})}{\hbar} \equiv \frac{\omega_{ex}}{2}\hat{\sigma}_x + ig(\bar{a}^* - \bar{a})\hat{\sigma}_z. \tag{100}$$

The normalized expectation value $\bar{a} = \langle\hat{a}\rangle/\sqrt{N}$ of the annihilation operator of a photon at temperature T can be determined to minimize the action, that is, $\partial\bar{\mathcal{S}}/\partial\text{Re}[\bar{a}] = 0$ and $\partial\bar{\mathcal{S}}/\partial\text{Im}[\bar{a}] = 0$. $\bar{a}$ acquires a non-zero value below T_c when $4g^2 > \omega_{ph}\omega_{ex}$ is satisfied ($\sqrt{N}\bar{a}$ gives a finite electric (displacement) field or vector potential even in the thermodynamic limit $N \rightarrow \infty$ if the atomic density is fixed). The above approximation is justified if the free energy $\bar{\mathcal{F}}_{Dicke}(T) \equiv -(k_B T/N)\ln\bar{\mathcal{Z}}_{Dicke}(T)$ per atom satisfies $\hbar\omega_{ph}/N \ll |\bar{\mathcal{F}}_{Dicke}(T)|$ in the thermodynamic limit[45,46,48,49].

Following the above treatment, we calculated the expectation values of the Er^{3+} spin and Fe^{3+} qAFM magnon operators in the extended Dicke Hamiltonian, Eq. (16), at a finite temperature. In the thermodynamic limit $N \rightarrow \infty$ the partition function $\mathcal{Z}(T) \equiv \text{Tr}[e^{-\hat{\mathcal{H}}/(k_B T)}]$ can be approximately evaluated by replacing the trace over the magnonic variables with an integral over c-numbers $\bar{a}_r, \bar{a}_i \in \mathbb{R}$,

giving $\hat{a}_\pi \to \sqrt{N}(\bar{a}_r + i\bar{a}_i)$, as

$$\bar{\mathcal{Z}}(T) \equiv \int \frac{d\bar{a}_r d\bar{a}_i}{\pi/N} \text{Tr}\left[e^{-\hat{\mathcal{H}}^{\text{eff}}(\bar{a}_r, \bar{a}_i)/(k_B T)}\right] \tag{101}$$

$$= \int \frac{d\bar{a}_r d\bar{a}_i}{\pi/N} e^{-\bar{\mathcal{S}}(\bar{a},T)/(k_B T)}, \tag{102}$$

where we define an effective Hamiltonian

$$\hat{\mathcal{H}}^{\text{eff}}(\bar{a}_r, \bar{a}_i)/\hbar \equiv N\omega_\pi(\bar{a}_r{}^2 + \bar{a}_i{}^2) + \omega_{\text{Er}}\hat{\Sigma}_x + \frac{4z_{\text{Er}}J_{\text{Er}}}{N\hbar}\left(\langle\hat{\Sigma}_x\rangle\hat{\Sigma}_x - \langle\hat{\Sigma}_z\rangle\hat{\Sigma}_z\right)$$

$$- \frac{2z_{\text{Er}}J_{\text{Er}}}{N\hbar}\left(\langle\hat{\Sigma}_x\rangle^2 - \langle\hat{\Sigma}_z\rangle^2\right) + 4g_x\bar{a}_r\hat{\Sigma}_x + 4g_z\bar{a}_i\hat{\Sigma}_z \tag{103}$$

by introducing the Fe^{3+} components $\langle\hat{\Sigma}_{x,z}\rangle$ of the mean fields of the Er^{3+} ensemble. The action in Eq. (102) is defined as follows.

$$\bar{\mathcal{S}}(\bar{a}_r, \bar{a}_i, T) \equiv -k_B T\ln\text{Tr}\left[e^{-\hat{\mathcal{H}}^{\text{eff}}(\bar{a}_r, \bar{a}_i)/(k_B T)}\right] \tag{104}$$

$$= N\left\{\hbar\omega_\pi(\bar{a}_r{}^2 + \bar{a}_i{}^2) - \frac{2z_{\text{Er}}J_{\text{Er}}}{N^2}\left(\langle\hat{\Sigma}_x\rangle^2 - \langle\hat{\Sigma}_z\rangle^2\right)\right\} - Nk_B T\ln\text{Tr}\left[e^{-\frac{\hat{\mathcal{H}}^a(\bar{a}_r,\bar{a}_i)}{k_B T}}\right]. \tag{105}$$

Here, we define an effective Hamiltonian per Er^{3+} spin as

$$\frac{\hat{\mathcal{H}}^a(\bar{a}_r, \bar{a}_i)}{\hbar} \equiv \frac{\omega_{\text{Er}}}{2}\hat{\sigma}_x + \frac{2z_{\text{Er}}J_{\text{Er}}}{N\hbar}\left(\langle\hat{\Sigma}_x^+\rangle\hat{\sigma}_x - \langle\hat{\Sigma}_z^-\rangle\hat{\sigma}_z\right) + 2g_x\bar{a}_r\hat{\sigma}_x + 2g_z\bar{a}_i\hat{\sigma}_z. \tag{106}$$

The site index i is omitted here because all the spins are identical. The action $\bar{\mathcal{S}}$ is minimized at $\partial\bar{\mathcal{S}}/\partial\bar{a}_r = 0$ and $\partial\bar{\mathcal{S}}/\partial\bar{a}_i = 0$, yielding

$$\omega_\pi\bar{a}_r + g_x\langle\hat{\sigma}_x\rangle = 0, \tag{107}$$

$$\omega_\pi\bar{a}_i + g_z\langle\hat{\sigma}_z\rangle = 0, \tag{108}$$

where the expectation values of the Pauli operators are defined for a given $\bar{a}_r$ and $\bar{a}_i$, as

$$\bar{\sigma}_\xi \equiv \langle\hat{\sigma}_\xi\rangle \equiv \frac{\text{Tr}[\hat{\sigma}_\xi e^{-\hat{\mathcal{H}}^a(\bar{a}_r,\bar{a}_i)/(k_B T)}]}{\text{Tr}[e^{-\hat{\mathcal{H}}^a(\bar{a}_r,\bar{a}_i)/(k_B T)}]}. \tag{109}$$

From Eqs. (107) and (108), the expectation values of the large spin operators can be expressed as

$$\langle\hat{\Sigma}_x\rangle = \frac{N}{2}\langle\hat{\sigma}_x\rangle = -\frac{N\omega_\pi}{2g_x}\bar{a}_r, \tag{110}$$

$$\langle\hat{\Sigma}_z\rangle = \frac{N}{2}\langle\hat{\sigma}_z\rangle = -\frac{N\omega_\pi}{2g_z}\bar{a}_i. \tag{111}$$

Substituting these into Eq. (106) gives

$$\frac{\hat{\mathcal{H}}^a(\bar{a}_r, \bar{a}_i)}{\hbar} = \frac{\omega_{\text{Er}}}{2}\hat{\sigma}_x + \left(2g_x - \frac{z_{\text{Er}}J_{\text{Er}}\omega_\pi}{\hbar g_x}\right)\bar{a}_r\hat{\sigma}_x + \left(2g_z + \frac{z_{\text{Er}}J_{\text{Er}}\omega_\pi}{\hbar g_z}\right)\bar{a}_i\hat{\sigma}_z. \tag{112}$$

By simultaneously solving Eqs. (107)–(109) and (112) for a given temperature, T, we obtain the thermal equilibrium values of the Er^{3+} spins $\bar{\sigma}_{x,z}$ and Fe^{3+} qAFM magnons $\bar{a}_{r,i}$. From Eqs. (60) and (68)–(71), the thermal equilibrium values of the Fe^{3+} spins can be obtained from those of the qAFM magnons $\bar{a}_{r,i}$ as

$$\bar{S}_x \equiv \langle\hat{S}_x^A\rangle = \langle\hat{S}_x^B\rangle = S\sin\beta_0 + \sqrt{2xS}\cos\beta_0\left(\frac{b+a}{d-c}\right)^{1/4}\bar{a}_r, \tag{113}$$

$$\bar{S}_y \equiv \langle\hat{S}_y^A\rangle = -\langle\hat{S}_y^B\rangle = -\sqrt{2xS}\left(\frac{d-c}{b+a}\right)^{1/4}\bar{a}_i, \tag{114}$$

$$\bar{S}_z \equiv -\langle\hat{S}_z^A\rangle = \langle\hat{S}_z^B\rangle = S\cos\beta_0 - \sqrt{2xS}\sin\beta_0\left(\frac{b+a}{d-c}\right)^{1/4}\bar{a}_r. \tag{115}$$

Condition for SRPT in extended Dicke Hamiltonian. To quantitatively evaluate the contributions of the Er^{3+}–magnon couplings and Er^{3+}–Er^{3+} exchange interactions to the LTPT, the condition for the SRPT in our extended Dicke Hamiltonian, Eq. (16), can be derived using the Holstein–Primakoff transformation[38–40]. $\hat{\Sigma}_{x,y,z}$ can be rewritten using the bosonic annihilation (creation) operator $\hat{b}$ ($\hat{b}^\dagger$) as

$$\hat{\Sigma}_x \to \hat{b}^\dagger\hat{b} - \frac{N}{2}, \tag{116}$$

$$\hat{\Sigma}_y \to \frac{\hat{b}^\dagger(N - \hat{b}^\dagger\hat{b})^{1/2} + (N - \hat{b}^\dagger\hat{b})^{1/2}\hat{b}}{2}, \tag{117}$$

$$\hat{\Sigma}_z \to \frac{\hat{b}^\dagger(N - \hat{b}^\dagger\hat{b})^{1/2} - (N - \hat{b}^\dagger\hat{b})^{1/2}\hat{b}}{i2}. \tag{118}$$

Further, all the operators are replaced by c-numbers $\bar{a}_r, \bar{a}_i, \bar{b} \in \mathbb{R}$ as

$$\hat{a} \to \sqrt{N}(\bar{a}_r + i\bar{a}_i), \tag{119}$$

$$\hat{b} \to i\sqrt{N}\bar{b}. \tag{120}$$

Subsequently, the Hamiltonian in Eq. (16) becomes

$$\frac{\hat{\mathcal{H}}}{N\hbar} \to \omega_\pi(\bar{a}_r{}^2 + \bar{a}_i{}^2) + \omega_{\text{Er}}\bar{b}^2 + \frac{4z_{\text{Er}}J_{\text{Er}}}{\hbar}\bar{b}^2(\bar{b}^2 - 1)$$

$$+ 2g_x\bar{a}_r(2\bar{b}^2 - 1) - 4g_z\bar{a}_i\bar{b}\sqrt{1 - \bar{b}^2} + \text{const.} \tag{121}$$

The ground state of the system should satisfy

$$\frac{1}{2}\frac{1}{\hbar N}\frac{\partial\mathcal{H}}{\partial\bar{a}_r} = \omega_\pi\bar{a}_r + g_x(2\bar{b}^2 - 1) = 0, \tag{122}$$

$$\frac{1}{2}\frac{1}{\hbar N}\frac{\partial\mathcal{H}}{\partial\bar{a}_i} = \omega_\pi\bar{a}_i - 2g_z\bar{b}\sqrt{1 - \bar{b}^2} = 0, \tag{123}$$

$$\frac{1}{2}\frac{1}{\hbar N}\frac{\partial\mathcal{H}}{\partial\bar{b}} = \omega_{\text{Er}}\bar{b} + \frac{4z_{\text{Er}}J_{\text{Er}}}{\hbar}\bar{b}(2\bar{b}^2 - 1) + 4g_x\bar{a}_r\bar{b} - 2g_z\bar{a}_i\frac{1 - 2\bar{b}^2}{\sqrt{1 - \bar{b}^2}} = 0. \tag{124}$$

Solving the first two equations, the Fe^{3+} qAFM magnon amplitudes can be expressed as

$$\bar{a}_r = -\frac{g_x}{\omega_\pi}(2\bar{b}^2 - 1), \tag{125}$$

$$\bar{a}_i = \frac{2g_z}{\omega_\pi}\bar{b}\sqrt{1 - \bar{b}^2}. \tag{126}$$

By substituting these expressions into Eq. (124), the following equation for the Er^{3+} amplitude can be obtained.

$$\left[\omega_{\text{Er}} - \frac{4g_z{}^2 - 4g_x{}^2}{\omega_\pi} - \frac{4z_{\text{Er}}J_{\text{Er}}}{\hbar} + \left(\frac{8g_z{}^2 - 8g_x{}^2}{\omega_\pi} + \frac{8z_{\text{Er}}J_{\text{Er}}}{\hbar}\right)\bar{b}^2\right]\bar{b} = 0. \tag{127}$$

For a real non-zero value of $\bar{b}$ to exist, the parameters must satisfy Eq. (22).

Data availability
Data plotted in Figs. 1–5 can be provided from the corresponding author on request.

Code availability
Code can be provided by the corresponding author on request.

References
1. Hepp, K. & Lieb, E. H. On the superradiant phase transition for molecules in a quantized radiation field: The Dicke maser model. *Ann. Phys. (N. Y.)* **76**, 360–404 (1973).
2. Wang, Y. K. & Hioe, F. T. Phase transition in the Dicke model of superradiance. *Phys. Rev. A.* **7**, 831–836 (1973).
3. Ciuti, C., Bastard, G. & Carusotto, I. Quantum vacuum properties of the intersubband cavity polariton field. *Phys. Rev. B.* **72**, 115303 (2005).
4. Forn-Díaz, P., Lamata, L., Rico, E., Kono, J. & Solano, E. Ultrastrong coupling regimes of light-matter interaction. *Rev. Mod. Phys.* **91**, 025005 (2019).
5. Frisk Kockum, A., Miranowicz, A., De Liberato, S., Savasta, S. & Nori, F. Ultrastrong coupling between light and matter. *Nat. Rev. Phys.* **1**, 19–40 (2019).
6. Dicke, R. H. Coherence in spontaneous radiation processes. *Phys. Rev.* **93**, 99–110 (1954).
7. Artoni, M. & Birman, J. L. Quantum-optical properties of polariton waves. *Phys. Rev. B.* **44**, 3736 (1991).
8. Artoni, M. & Birman, J. L. Polariton squeezing: Theory and proposed experiment. *Quantum Opt. J. Eur. Opt. Soc. Part B.* **1**, 91 (1989).
9. Schwendimann, P. & Quattropani, A. Nonclassical properties of polariton states. *Europhys. Lett.* **17**, 355 (1992).

10. Schwendimann, P. & Quattropani, A. Nonclassical properties of polariton states. *Europhys. Lett.* **18**, 281 (1992).

11. Quattropani, A. & Schwendimann, P. Polariton squeezing in microcavities. *Phys. Status. Solidi.* **242**, 2302–2314 (2005).

12. Makihara, T. et al. Ultrastrong magnon–magnon coupling dominated by antiresonant interactions. *Nat. Commun.* **12**, 3115 (2021).

13. Hayashida, K. et al. Perfect intrinsic squeezing at the superradiant phase transition critical point. Preprint at *arXiv: 2009.02630* [quant-ph] (2020).

14. Black, A. T., Chan, H. W. & Vuletić, V. Observation of collective friction forces due to spatial self-organization of atoms: From Rayleigh to Bragg scattering. *Phys. Rev. Lett.* **91**, 203001 (2003).

15. Baumann, K., Guerlin, C., Brennecke, F. & Esslinger, T. Dicke quantum phase transition with a superfluid gas in an optical cavity. *Nature* **464**, 1301–1306 (2010).

16. Zhiqiang, Z. et al. Nonequilibrium phase transition in a spin-1 Dicke model. *Optica.* **4**, 424 (2017).

17. Kirton, P., Roses, M. M., Keeling, J. & Dalla Torre, E. G. Introduction to the Dicke model: From equilibrium to nonequilibrium, and vice versa. *Adv. Quantum Technol.* **2**, 1800043 (2019).

18. Nataf, P. & Ciuti, C. Vacuum degeneracy of a circuit QED system in the ultrastrong coupling regime. *Phys. Rev. Lett.* **104**, 23601 (2010).

19. Nataf, P. & Ciuti, C. No-go theorem for superradiant quantum phase transitions in cavity QED and counter-example in circuit QED. *Nat. Commun.* **1**, 72 (2010).

20. Viehmann, O., Von Delft, J. & Marquardt, F. Superradiant phase transitions and the standard description of circuit QED. *Phys. Rev. Lett.* **107**, 113602 (2011).

21. Ciuti, C. & Nataf, P. Comment on "Superradiant phase transitions and the standard description of circuit QED". *Phys. Rev. Lett.* **109**, 179301 (2012).

22. Nataf, P., Baksic, A. & Ciuti, C. Double symmetry breaking and two-dimensional quantum phase diagram in spin-boson systems. *Phys. Rev. A.* **86**, 013832 (2012).

23. Jaako, T., Xiang, Z. L., Garcia-Ripoll, J. J. & Rabl, P. Ultrastrong-coupling phenomena beyond the Dicke model. *Phys. Rev. A.* **94**, 033850 (2016).

24. Bamba, M., Inomata, K. & Nakamura, Y. Superradiant phase transition in a superconducting circuit in thermal equilibrium. *Phys. Rev. Lett.* **117**, 173601 (2016).

25. Herrmann, G. F. Magnetic resonances and susceptibility in orthoferrites. *Phys. Rev.* **133**, A1334 (1964).

26. Zhang, X. X. et al. Magnetic behavior and complete high-field magnetic phase diagram of the orthoferrite $ErFeO_3$. *Phys. Rev. B.* **100**, 054418 (2019).

27. Gorodetsky, G. et al. Magnetic structure of $ErFeO_3$ below 4.5 K. *Phys. Rev. B.* **8**, 3398–3404 (1973).

28. Klochan, V. A., Kovtun, N. M. & Khmara, V. M. Low-temperature spin configuration of iron ions in erbium orthoferrite. *Zh. Eksp. Teor. Fiz.* **68**, 721–726 (1975).

29. Kadomtseva, A. M., Krynetskil, I. B. & Matveev, V. M. Nature of the spontaneous and field-induced low-temperature orientational transitions in erbium orthoferrite. *Sov. Phys. JETP.* **52**, 732–737 (1980).

30. Vitebskii, I. M. & Yablonskii, D. A. Theory of low-temperature spin reorientation in $ErFeO_3$. *Sov. Phys. Solid. State.* **20**, 1327–1332 (1978).

31. Li, X. et al. Observation of Dicke cooperativity in magnetic interactions. *Science.* **361**, 794–797 (2018).

32. Wood, D. L., Remeika, J. P., Holmes, L. M. & Gyorgy, E. M. Effect of Y and Bi Substitution on Spin Reorientation and Optical Absorption in $ErFeO_3$. *J. Appl. Phys.* **40**, 1245–1246 (1969).

33. Herrmann, G. Resonance and high frequency susceptibility in canted antiferromagnetic substances. *J. Phys. Chem. Solids.* **24**, 597–606 (1963).

34. Bamba, M., Li, X. & Kono, J. Terahertz strong-field physics without a strong external terahertz field. In *Proc. SPIE 10916,Ultrafast Phenom. Nanophotonics XXIII* (eds Betz, M. & Elezzabi, A. Y.) 1091605 https://doi.org/10.1117/12.2512794 (2019).

35. Mazza, G. & Georges, A. Superradiant quantum materials. *Phys. Rev. Lett.* **122**, 017401 (2019).

36. Andolina, G. M., Pellegrino, F. M. D., Giovannetti, V., MacDonald, A. H. & Polini, M. Cavity quantum electrodynamics of strongly correlated electron systems: A no-go theorem for photon condensation. *Phys. Rev. B.* **100**, 121109 (2019).

37. Nataf, P., Champel, T., Blatter, G. & Basko, D. M. Rashba Cavity QED: A route towards the superradiant quantum phase transition. *Phys. Rev. Lett.* **123**, 207402 (2019).

38. Holstein, T. & Primakoff, H. Field dependence of the intrinsic Domain Magnetization of a ferromagnet. *Phys. Rev.* **58**, 1098–1113 (1940).

39. Emary, C. & Brandes, T. Quantum chaos triggered by precursors of a quantum phase transition: The Dicke model. *Phys. Rev. Lett.* **90**, 044101 (2003).

40. Emary, C. & Brandes, T. Chaos and the quantum phase transition in the Dicke model. *Phys. Rev. E.* **67**, 066203 (2003).

41. Gehring, G. A. & Gehring, K. A. Co-operative Jahn-Teller effects. *Reports Prog. Phys.* **38**, 1–89 (1975).

42. Kugel', K. I. & Khomskii, D. I. The Jahn-Teller effect and magnetism: Transition metal compounds. *Sov. Phys. Uspekhi.* **25**, 231–256 (1982).

43. Rzażewski, K., Wódkiewicz, K. & Żakowicz, W. Phase transitions, two-level atoms, and the A^2 term. *Phys. Rev. Lett.* **35**, 432–434 (1975).

44. Knight, J. M., Aharonov, Y. & Hsieh, G. T. C. Are super-radiant phase transitions possible? *Phys. Rev. A.* **17**, 1454–1462 (1978).

45. Bialynicki-Birula, I. & Rzażewski, K. No-go theorem concerning the superradiant phase transition in atomic systems. *Phys. Rev. A.* **19**, 301–303 (1979).

46. Gawedzki, K. & Rzażewski, K. No-go theorem for the superradiant phase transition without dipole approximation. *Phys. Rev. A.* **23**, 2134–2136 (1981).

47. Hepp, K., Lieb, E. H., Field, R. & Etudes, K. Equilibrium statistical mechanics of matter interacting with the quantized radiation field. *Phys. Rev. A.* **8**, 2517–2525 (1973).

48. van Hemmen, J. L. & Rzażewski, K. On the thermodynamic equivalence of the Dicke maser model and a certain spin system. *Phys. Lett. A.* **77**, 211–213 (1980).

49. Bamba, M. & Imoto, N. Circuit configurations which may or may not show superradiant phase transitions. *Phys. Rev. A.* **96**, 053857 (2017).

50. Keeling, J. Coulomb interactions, gauge invariance, and phase transitions of the Dicke model. *J. Phys. Condens. Matter.* **19**, 295213 (2007).

51. Vukics, A. & Domokos, P. Adequacy of the Dicke model in cavity QED: A counter-no-go statement. *Phys. Rev. A.* **86**, 53807 (2012).

52. Vukics, A., Grießer, T. & Domokos, P. Elimination of the A-square problem from cavity QED. *Phys. Rev. Lett.* **112**, 73601 (2014).

53. Bamba, M. & Ogawa, T. Stability of polarizable materials against superradiant phase transition. *Phys. Rev. A.* **90**, 063825 (2014).

54. Vukics, A., Grießer, T. & Domokos, P. Fundamental limitation of ultrastrong coupling between light and atoms. *Phys. Rev. A.* **92**, 43835 (2015).

55. Grießer, T., Vukics, A. & Domokos, P. Depolarization shift of the superradiant phase transition. *Phys. Rev. A.* **94**, 033815 (2016).

56. Hagenmüller, D. & Ciuti, C. Cavity QED of the graphene cyclotron transition. *Phys. Rev. Lett.* **109**, 267403 (2012).

57. Chirolli, L., Polini, M., Giovannetti, V. & MacDonald, A. H. Drude weight, cyclotron resonance, and the Dicke model of graphene cavity QED. *Phys. Rev. Lett.* **109**, 267404 (2012).

58. Andolina, G. M., Pellegrino, F. M. D., Giovannetti, V., MacDonald, A. H. & Polini, M. Theory of photon condensation in a spatially varying electromagnetic field. *Phys. Rev. B.* **102**, 125137 (2020).

59. Guerci, D., Simon, P. & Mora, C. Superradiant phase transition in electronic systems and emergent topological phases. *Phys. Rev. Lett.* **125**, 257604 (2020).

60. Zhang, X., Zou, C. L., Jiang, L. & Tang, H. X. Strongly coupled magnons and cavity microwave photons. *Phys. Rev. Lett.* **113**, 156401 (2014).

61. Goryachev, M. et al. High-cooperativity cavity QED with magnons at microwave frequencies. *Phys. Rev. Appl.* **2**, 54002 (2014).

62. Bourhill, J., Kostylev, N., Goryachev, M., Creedon, D. L. & Tobar, M. E. Ultrahigh cooperativity interactions between magnons and resonant photons in a YIG sphere. *Phys. Rev. B.* **93**, 144420 (2016).

63. Kostylev, N., Goryachev, M. & Tobar, M. E. Superstrong coupling of a microwave cavity to yttrium iron garnet magnons. *Appl. Phys. Lett.* **108**, 062402 (2016).

64. Flower, G., Goryachev, M., Bourhill, J. & Tobar, M. E. Experimental implementations of cavity-magnon systems: From ultra strong coupling to applications in precision measurement. *New J. Phys.* **21**, 095004 (2019).

65. Flower, G., Bourhill, J., Goryachev, M. & Tobar, M. E. Broadening frequency range of a ferromagnetic axion haloscope with strongly coupled cavity-magnon polaritons. *Phys. Dark Universe* **25**, 100306 (2019).

66. Macneill, D. et al. Gigahertz frequency antiferromagnetic resonance and strong magnon–magnon coupling in the layered crystal $CrCl_3$. *Phys. Rev. Lett.* **123**, 47204 (2019).

67. Liensberger, L. et al. Exchange-enhanced ultrastrong magnon–magnon coupling in a compensated ferrimagnet. *Phys. Rev. Lett.* **123**, 117204 (2019).

68. Loos, J. On the fluctuations and phase transitions in Dicke-like models. *Phys. Status Solidi* **123**, 595–603 (1984).

69. Larson, J. Jahn-Teller systems from a cavity QED perspective. *Phys. Rev. A* **78**, 33833 (2008).

70. Chesnut, D. B. Instability of a Linear Spin Array: Application to Würster's Blue Perchlorate. *J. Chem. Phys.* **45**, 4677–4681 (1966).

71. Kobayashi, K. K. Phase Transition in a Coupled Phonon-Linear Heisenberg Chain System. *J. Phys. Soc. Japan.* **44**, 1869–1872 (1978).

72. Loos, J. On a ferromagnet coupled to the paramagnetic system: Fluctuations and spin reorientation. *Phys. status solidi.* **114**, 319–329 (1982).

73. Pálová, L., Chandra, P. & Coleman, P. Quantum critical paraelectrics and the Casimir effect in time. *Phys. Rev. B.* **79**, 075101 (2009).

74. Larson, J. & Irish, E. K. Some remarks on 'superradiant' phase transitions in light-matter systems. *J. Phys. A Math. Theor.* **50**, 174002 (2017).

75. Shapiro, D. S., Pogosov, W. V. & Lozovik, Y. E. Hierarchy of universal behaviors in generalized Dicke model near the superradiant phase transition. *Phys. Rev. A* **102**, 023703 (2020).
76. Marquez Peraca, N. et al. Terahertz magnon spectroscopy mapping of the low-temperature phases of $Er_xY_{1-x}FeO_3$. *Proceedings of 2020 Conference on Lasers and Electro-Optics (CLEO)*, paper FM4D.5, 10–15 May 2020 (Washington, D.C., 2020).
77. Riek, C. et al. Direct sampling of electric-field vacuum fluctuations. *Science* **350**, 420 (2015).
78. Benea-Chelmus, I. C., Settembrini, F. F., Scalari, G. & Faist, J. Electric field correlation measurements on the electromagnetic vacuum state. *Nature.* **568**, 202 (2019).

Acknowledgements

Author contributions

M.B. performed theoretical calculations and largely wrote the manuscript. X.L., N.M.P., and J.K. contributed to the consistency with terahertz magnetospectroscopy experiments. All authors discussed the confirmation of the magnetic SRPT and commented on the manuscript.

Competing interests

The authors declare no competing interests.

Additional information

Supplementary information The online version contains supplementary material available at https://doi.org/10.1038/s42005-021-00785-z.

Correspondence and requests for materials should be addressed to Motoaki Bamba.

Peer review information *Communications Physics* thanks the anonymous reviewers for their contribution to the peer review of this work.

Reprints and permission information is available at http://www.nature.com/reprints

Publisher's note Springer Nature remains neutral with regard to jurisdictional claims in published maps and institutional affiliations.